Improved strong-field approximation and quantum-orbit theory: Application to ionization by a bicircular laser field

D. B. Milošević[1,2,3] and W. Becker[3,4]

[1]*Faculty of Science, University of Sarajevo, Zmaja od Bosne 35, 71000 Sarajevo, Bosnia and Herzegovina*

[2]*Academy of Sciences and Arts of Bosnia and Herzegovina, Bistrik 7, 71000 Sarajevo, Bosnia and Herzegovina*

[3]*Max-Born-Institut, Max-Born-Straße 2a, 12489 Berlin, Germany*

[4]*National Research Nuclear University MEPhI, Kashirskoe Shosse 31, 115409 Moscow, Russia*

(Received 12 April 2016; published 20 June 2016)

A theory of above-threshold ionization of atoms by a strong laser field is formulated. Two versions of the strong-field approximation (SFA) are considered, the direct SFA and the improved SFA, which do not and do, respectively, take into account rescattering of the freed electron off the parent ion. The atomic bound state is included in two different ways: as an expansion in terms of Slater-type orbitals or as an asymptotic wave function. Even though we are using the single-active-electron approximation, multielectron effects are taken into account in two ways: by a proper choice of the ground state and by an adequate definition of the ionization rate. For the case of the asymptotic bound-state wave functions, using the saddle-point method, a simple expression for the T-matrix element is derived for both the direct and the improved SFA. The theory is applied to ionization by a bicircular field, which consists of two coplanar counterrotating circularly polarized components with frequencies that are integer multiples of a fundamental frequency ω. Special emphasis is on the ω-2ω case. In this case, the threefold rotational symmetry of the field carries over to the velocity map of the liberated electrons, for both the direct and the improved SFA. The results obtained are analyzed in detail using the quantum-orbit formalism, which gives good physical insight into the above-threshold ionization process. For this purpose, a specific classification of the saddle-point solutions is introduced for both the backward-scattered and the forward-scattered electrons. The high-energy backward-scattering quantum orbits are similar to those discovered for high-order harmonic generation. The short forward-scattering quantum orbits for a bicircular field are similar to those of a linearly polarized field. The conclusion is that these orbits are universal, i.e., they do not depend much on the shape of the laser field.

DOI: 10.1103/PhysRevA.93.063418

I. INTRODUCTION

Strong-field physics explores the interaction of intense electromagnetic fields with matter. The advances of ultrafast laser science and strong-field physics have led to the possibility of tracking the electronic and structural dynamics on the subfemtosecond time scale, which has opened up a new area of science: attoscience (see, for example, the review articles in [1–13] and references therein). In this context, two laser-induced processes are particularly important: high-order harmonic generation (HHG) and above-threshold ionization (ATI). In the ATI process the atom or molecule is ionized by the strong laser field. During ATI more photons are absorbed from the laser field than is necessary for ionization and the emitted electron spectrum consists of peaks separated by the photon energy $\hbar\omega$. If the oscillating laser field is linearly polarized, the ionized electron can be driven back by the laser field exactly to the position of its parent ion. If this electron recombines with the ion, its entire energy is emitted as one high-energy photon in this so-called HHG process. The returning electron can also elastically rescatter off the parent ion, move away from it, and reach the detector with a higher energy: This is the high-order ATI (HATI) process. As described above, the so-called three-step model (ionization, propagation, and rescattering or recombination with high-harmonic emission) [14] was crucial for the development of strong-field physics and attoscience.

Atomic and molecular processes in a strong field are quantum-mechanical processes. Having in mind wave-particle duality, the classical trajectories described above should be replaced by electronic wave packets. Feynman's path integral is very suitable for the description of HHG and HATI processes [15–18]. A realization of this approach is the so-called quantum-orbit theory [19–22]. In this formalism, the electron does not have to start with zero velocity and then follow only one classical trajectory and return to the parent ion. In the Feynman path-integral approach and quantum-orbit theory, the transition amplitude is the coherent sum of many different paths, expressed as $\sum_s A_s \exp(iS_s)$, with S_s the action along the sth path. In laser-induced processes the times (ionization and rescattering times for HATI) that enter the formalism are complex and so are the corresponding trajectories. A visualization of such processes can be accomplished by projecting these trajectories onto the real plane.

The quantum-orbit formalism described above is not restricted to linearly polarized fields. In Refs. [15,20,23] elliptically polarized laser fields were extensively considered. If the polarization is not linear, an electron released with zero velocity will not normally be driven into an exact recollision. However, HHG and ATI still occur, though with decreasing yield for increasing ellipticity. This is possible since the electronic wave packet has a distribution of transverse momenta and with the appropriate magnitude of the latter the electron does recollide. However, the larger this transverse momentum has to be the more the HHG or ATI yield will be suppressed.

One such nonlinearly polarized field, the bicircular field, has recently generated much interest. In fact, in [24] it was

observed that strong high-harmonic emission can be achieved using a field that consists of two coplanar counterrotating circularly polarized fields having the frequencies ω and 2ω. Calculations based on the zero-range potential model have confirmed this [25]. The HHG process in a bicircular field and a static magnetic field was considered in [26]. The HHG process with the bicircular field was explained using a semiclassical three-step model based on the quantum-orbit formalism [27]. The two-dimensional electron trajectories responsible for this process were clearly identified. It was found that the harmonic-emission efficiency is very high [28], that the harmonics are circularly polarized with alternating helicities, and that the polarization of an attosecond pulse train generated by the superposition of several such harmonics is unusual [29]. High-order harmonic generation by a bicircular field with frequencies $r\omega$ and $s\omega$, with r and s integers, was considered in detail in [30]. However, only in [31] was it shown experimentally that the high-order harmonics are really circularly polarized. Since circularly polarized radiation in this frequency range thus far has only been available at large facilities, this scheme is attracting a great deal of attention [32–38] and is becoming a very active area of research [39,40].

The (H)ATI process by a bicircular field was considered in Ref. [41], where a superposition of two counterrotating circularly polarized pulses, having the same frequency, was considered. One of these pulses was long while the other one was a few-cycle pulse. It was shown that high-energy electrons, generated in ionization by such a combination of pulses, are emitted in a direction correlated with the carrier-envelope phase. Angle-resolved electron energy spectra in strong-field ionization by a bicircular field of arbitrary frequencies $r\omega$ and $s\omega$ were analyzed in [42]. For the case where $r = 1$ and $s = 2$, the predicted three-lobed shape of these spectra was recently confirmed experimentally [43]. In addition, in [43] low-energy features of the electron spectra due to Coulomb-field-enhanced rescattering were observed and confirmed in numerical calculations. However, high-energy features, also visible in the observed spectra presented in [43], were not explained. High-energy spectra have recently been considered theoretically in [44] and experimentally in [45]. The low-energy features of the observed spectra can be related to the so-called low-energy structures (LESs) in ATI by a linearly polarized laser field. These were discovered in [46,47] and have attracted much attention because they cannot be explained by the standard strong-field approximation (SFA). However, the improved SFA (ISFA), which includes rescattering, successfully describes both the LES [48] and its subsequently observed off-axis extension [49] as well as an off-axis V structure [50] (see also the more recent papers [12,51–53] and references therein).

The main body of this paper is divided into four sections. Section II consists of six subsections in which we define the transition matrix element, introduce the ISFA and the saddle-point method (SPM), define our bicircular field, present the classical cutoff law, and consider symmetries of the matrix elements. Compared with earlier work, the SPM is modified so that it can be applied to the asymptotic states of the inert-gas atoms. In Sec. III we separately present the results obtained using the direct SFA and using the ISFA, which takes into account rescattering. Section IV is devoted to the quantum orbits and their visualization in the form of two-dimensional electron trajectories. Finally, Sec. V contains our concluding remarks and some discussion. The atomic system of units is used.

II. THEORY

A. Transition matrix element

We denote the total Hamiltonian of an atom (or a negative ion) interacting with the laser field by

$$H(t) = H_0 + V_{\rm le}(t) + V(\mathbf{r}), \tag{1}$$

where (in atomic units) $H_0 = -\nabla^2/2$, $\boldsymbol{\nabla} \equiv \partial/\partial\mathbf{r}$, $V_{\rm le}(t)$ is the laser-field–electron interaction, and $V(\mathbf{r}) = V_C(r) + V_{\rm sh}(r)$, with $V_C(r) = -Z/r$ ($Z = 1$ for atoms and $Z = 0$ for negative ions) the Coulomb interaction and $V_{\rm sh}(r)$ a short-range interaction. The total time-evolution operator $U(t,t')$ corresponds to the Hamiltonian $H(t)$, while the evolution operators $U_{\rm le}$ and U_V correspond to the Hamiltonians $H_{\rm le} = H_0 + V_{\rm le}$ and $H_V = H_0 + V$, respectively. They satisfy the Dyson equations

$$U(t,\tau) = U_{\rm le}(t,\tau) - i\int_\tau^t d\tau' U(t,\tau')V(\mathbf{r})U_{\rm le}(\tau',\tau), \tag{2}$$

$$U(t,t') = U_V(t,t') - i\int_{t'}^t d\tau\, U(t,\tau)V_{\rm le}(\tau)U_V(\tau,t'). \tag{3}$$

In length gauge and dipole approximation we have

$$V_{\rm le}(t) = \mathbf{r}\cdot\mathbf{E}(t), \tag{4}$$

$$U_{\rm le}(t,t') = \int d\mathbf{k}|\chi_{\mathbf{k}}(t)\rangle\langle\chi_{\mathbf{k}}(t')|, \tag{5}$$

$$|\chi_{\mathbf{k}}(t)\rangle = |\mathbf{k} + \mathbf{A}(t)\rangle \exp[-iS_{\mathbf{k}}(t)], \tag{6}$$

where $\mathbf{E}(t) = -d\mathbf{A}(t)/dt$ is the electric-field vector, $U_{\rm le}(t,t')$ is the Volkov time-evolution operator, $|\chi_{\mathbf{k}}(t)\rangle$ are the Volkov states, $dS_{\mathbf{k}}(t)/dt = [\mathbf{k} + \mathbf{A}(t)]^2/2$, and $|\mathbf{q}\rangle$ is a plane-wave ket such that $\langle\mathbf{r}|\mathbf{q}\rangle = (2\pi)^{-3/2}\exp(i\mathbf{q}\cdot\mathbf{r})$.

We consider an ionization (detachment) process in which the interaction with the laser field is turned off at times t and t' so that the states $|\psi_{\mathbf{p}}(t)\rangle = |\psi_{\mathbf{p}}\rangle e^{-iE_{\mathbf{p}}t}$ and $|\psi_i(t')\rangle = |\psi_i\rangle e^{-iE_it'}$ are mutually orthogonal eigenstates of the Hamiltonian H_V with the eigenenergies $E_{\mathbf{p}} = \mathbf{p}^2/2$ and $E_i = -I_p < 0$, respectively. The quantity E_i denotes the atomic or negative-ion binding energy, while I_p is the atomic ionization potential or the negative-ion electron affinity. The transition matrix element from the initial bound state $|\psi_i(t')\rangle$ to the final state $|\psi_{\mathbf{p}}(t)\rangle$ of the electron having the asymptotic momentum $\mathbf{p}$ and energy $E_{\mathbf{p}}$ is

$$M_{\mathbf{p}i}(t,t') = \langle\psi_{\mathbf{p}}(t)|U(t,t')|\psi_i(t')\rangle. \tag{7}$$

Introducing Eq. (3) into (7) and replacing in the resulting equation the operator $U(t,\tau)$ with (2), we obtain

$$M_{\mathbf{p}i}(t,t') = M^D_{\mathbf{p}i}(t,t') + M^R_{\mathbf{p}i}(t,t'), \tag{8}$$

$$M^D_{\mathbf{p}i}(t,t') = -i\int_{t'}^t d\tau\langle\psi_{\mathbf{p}}(t)|U_{\rm le}(t,\tau)V_{\rm le}(\tau)|\psi_i(\tau)\rangle, \tag{9}$$

$$M^R_{\mathbf{p}i}(t,t') = (-i)^2\int_{t'}^t d\tau\int_\tau^t d\tau'\langle\psi_{\mathbf{p}}(t)|U(t,\tau') \times V(\mathbf{r})U_{\rm le}(\tau',\tau)V_{\rm le}(\tau)|\psi_i(\tau)\rangle. \tag{10}$$

The superscripts D and R stand, respectively, for the direct and the rescattered (on the potential V) parts of the transition amplitude.

The differential ionization probability for emission of an electron with the energy $E_{\mathbf{p}}$ into the solid-angle element $d\Omega_{\hat{\mathbf{p}}}$ for a laser pulse having duration T_p is given by [3]

$$W_{\mathbf{p}i}(T_p) = \left| M_{\mathbf{p}i}\left(\frac{T_p}{2}, -\frac{T_p}{2}\right)\right|^2 \frac{d\mathbf{p}}{d\Omega_{\hat{\mathbf{p}}} dE_{\mathbf{p}}}. \quad (11)$$

For an infinitely long ($T_p \to \infty$) periodic laser field with the period $T = 2\pi/\omega$, using relations $\int_{-\infty}^{\infty} dt f(t) = \sum_{n=-\infty}^{\infty} \int_0^T dt f(t+nT)$, $\sum_{n=-\infty}^{\infty} e^{inET} = \omega \sum_{n=-\infty}^{\infty} \delta(E - n\omega)$, and $S_{\mathbf{p}}(t+T) = S_{\mathbf{p}}(t) + (E_{\mathbf{p}} + U_p)T$, where $f(t)$ is an arbitrary function and $U_p = \int_0^T \mathbf{A}^2(\tau) d\tau/(2T)$ is the ponderomotive energy, the transition amplitude can be expressed via the T-matrix element by the formula (see, for example, Sec. III C in [54])

$$M_{\mathbf{p}i} = -2\pi i \sum_n \delta(E_{\mathbf{p}} - E_i + U_p - n\omega) T_{\mathbf{p}i}(n). \quad (12)$$

Here we have introduced the notation that omitting the arguments t and t' in $M_{\mathbf{p}i}(t,t')$ means that they take their asymptotic values so that $M_{\mathbf{p}i} \equiv M_{\mathbf{p}i}(\infty, -\infty)$. The argument of the δ function displays energy conservation. Explicit expressions for the T-matrix element in the form of the integral over one optical cycle are given in the next subsection. Using the relation $2\pi\delta(0) = T_p$ (for $T_p \to \infty$), from Eqs. (11) and (12) for the differential ionization (detachment) rate we obtain

$$\lim_{T_p\to\infty} \frac{W_{\mathbf{p}i}(T_p)}{T_p} = \sum_n w_{\mathbf{p}i}(n) \delta(E_{\mathbf{p}} - E_i + U_p - n\omega), \quad (13)$$

where

$$w_{\mathbf{p}i}(n) = 2\pi p |T_{\mathbf{p}i}(n)|^2 \quad (14)$$

is the differential ionization (detachment) rate with absorption of n photons.

Our ground-state wave functions are given in the form of the ith atomic orbitals, obtained by solving the Roothan-Hartree-Fock equations [55]. In spherical coordinates, with the z axis as the quantization axis, they are given by

$$\psi_{ilm}(\mathbf{r}) = \langle r\theta\phi|\psi_{ilm}\rangle = R_{il}(r) Y_{lm}(\theta,\phi), \quad (15)$$

where $Y_{lm}(\theta,\phi) = \langle\theta\phi|lm\rangle$ are the normalized spherical harmonics in complex form, while the radial wave functions $R_{il}(r)$ are expanded in terms of basis functions (for example, Slater-type orbitals [55,56]) or represented by the asymptotic wave functions [56–58]. In the case of the expansion in Slater-type orbitals, the radial wave function is

$$R_{il}(r) = \sum_a C_a \frac{(2\zeta_a)^{n_a+1/2}}{\sqrt{(2n_a)!}} r^{n_a-1} e^{-\zeta_a r}, \quad (16)$$

where n_a and l are the quantum numbers of the electron and the parameters C_a and ζ_a characterize the radial distribution of the electron density and can be found tabulated in [55,56]. For the inert gases considered in the present paper we will use the orbitals given in Table I. Since we are using the length gauge, the interaction (4) emphasizes large distances where the bound-state wave functions have well-defined asymptotic behavior and the approximation

$$R_{il}(r) \approx A r^{\nu-1} \exp(-\kappa r), \quad r \gg 1 \quad (17)$$

is well justified [57]. The constant A is tabulated in [56,59,60], $\nu = Z/\kappa$, and $\kappa = \sqrt{2I_p}$. For the inert gases the corresponding values of I_p and A are given in Table I.

TABLE I. Ground-state configurations of valence electrons (the number of the used Slater-type orbitals is given in parentheses), ionization potentials, and asymptotic expansion coefficients A for inert atomic gases [56,59,60].

Atom	Configuration	I_p (eV)	A (a.u.)
He	$1s(5)$	24.59	2.87
Ne	$2p(4)$	21.56	2.1
Ar	$2p(2) + 3p(2)$	15.76	2.51
Kr	$3p(2) + 4p(2)$	14.00	2.59
Xe	$3p(1) + 4p(2) + 5p(2)$	12.13	2.72

We are using the single-active-electron approximation. However, different electrons from the ground-state configuration of the atom (negative ion) can play the role of this active electron. Denoting by N_e the number of equivalent electrons in the ionizing shell of the target and averaging over the possible values of m (there are $2l+1$ values of m, $m = -l, \ldots, l$), we obtain that Eq. (14) should be replaced by

$$\bar{w}_{\mathbf{p}i}(n) = \frac{N_e}{2l+1} \sum_{m=-l}^{l} w_{\mathbf{p}ilm}(n). \quad (18)$$

We neglect the effect of the fine-structure splitting [61] and the appearance of spin-orbit sublevels (see [62] and references therein for a more general definition). We usually consider the case of closed subshells specified by the orbital quantum number l. This subshell has $2l+1$ orbitals specified by m. Each orbital can be occupied by two electrons having different values of the spin projections. Therefore, in this case we have $N_e = 2(2l+1)$ in Eq. (18). For He we have $l = m = 0$, while for other inert gases we have $l = 1$, so three terms ($m = 0, \pm 1$) have to be taken into account in Eq. (18).

B. Improved strong-field approximation

We will first analyze the term $M^D_{\mathbf{p}i}$, which corresponds to direct ATI or direct above-threshold detachment (ATD). If in Eq. (9) we approximate $\langle\psi_{\mathbf{p}}(t)|U_{\rm le}(t,\tau)$ with $\langle\chi_{\mathbf{p}}(\tau)|$, i.e., with the Volkov state that corresponds to the electron having the asymptotic momentum $\mathbf{p}$ outside the laser field, we obtain the standard SFA for direct ATI (Keldysh-Faisal-Reiss [63] theory or the direct SFA):

$$M^{\rm SFA}_{\mathbf{p}i}(t,t') = -i \int_{t'}^{t} d\tau \langle\chi_{\mathbf{p}}(\tau)|V_{\rm le}(\tau)|\psi_i(\tau)\rangle. \quad (19)$$

In this case, for a T-periodic laser field and in the limits $t \to \infty$ and $t' \to -\infty$, we obtain the result (14), where the T-matrix element for the direct ATI (ATD) is given by [64]

$$T^{\rm SFA}_{\mathbf{p}i}(n) = \int_0^T \frac{dt_0}{T} \langle\mathbf{p} + \mathbf{A}(t_0)|V_{\rm le}(t_0)|\psi_i\rangle e^{i[S_{\mathbf{p}}(t_0) + I_p t_0]}. \quad (20)$$

Using the energy-conservation condition $n\omega = E_{\mathbf{p}} + I_p + U_p$ we can rewrite the exponent in Eq. (20) as $S_{\mathbf{p}}(t_0) + I_p t_0 = \mathbf{p}\cdot\boldsymbol{\alpha}(t_0) + \mathcal{U}_1(t_0) + n\omega t_0$, where $\mathbf{A}(t) = d\boldsymbol{\alpha}(t)/dt$ and $\mathcal{U}_1(t) = \int^t dt' \mathbf{A}(t')^2/2 - U_p t$. This one-dimensional integral over the ionization time t_0 can be calculated numerically.

The improved SFA can be obtained by approximating in the rescattering matrix element (10) the bra vector $\langle\psi_{\mathbf{p}}(t)|U(t,\tau')$ by the Volkov vector $\langle\chi_{\mathbf{p}}(\tau')|$. Then, using Eq. (5), the rescattering matrix element (10) can be approximated by

$$M^R_{\mathbf{p}i}(t,t') \approx (-i)^2 \int_{t'}^{t} d\tau \int d\mathbf{k} \int_{\tau}^{t} d\tau' \langle\chi_{\mathbf{p}}(\tau')|V(\mathbf{r})|\chi_{\mathbf{k}}(\tau')\rangle \times \langle\chi_{\mathbf{k}}(\tau)|V_{\rm le}(\tau)|\psi_i(\tau)\rangle. \quad (21)$$

For a T-periodic laser field, in the limits $t \to \infty$ and $t' \to -\infty$, for the corresponding T-matrix element we get

$$T^R_{\mathbf{p}i}(n) \approx -i \int_0^T \frac{dt}{T} \int d\mathbf{k} \langle\chi_{\mathbf{p}}(t)|V(\mathbf{r})|\chi_{\mathbf{k}}(t)\rangle \times \int_{-\infty}^{t} dt_0 \langle\chi_{\mathbf{k}}(t_0)|V_{\rm le}(\tau)|\psi_i(t_0)\rangle. \quad (22)$$

Using the SPM, the integral over the intermediate electron momenta $\mathbf{k}$ can be (approximately [65]) solved and we obtain the ISFA T-matrix element

$$T^{\rm ISFA}_{\mathbf{p}i}(n) = -i \int_0^T \frac{dt}{T} \int_{-\infty}^{t} dt_0 \left[\frac{2\pi}{i(t-t_0)}\right]^{3/2} \times \langle\mathbf{p}|V(\mathbf{r})|\mathbf{k}_{\rm st}\rangle \langle\mathbf{k}_{\rm st} + \mathbf{A}(t_0)|V_{\rm le}(t_0)|\psi_i\rangle \times e^{i[S_{\mathbf{p}}(t) - S_{\mathbf{k}_{\rm st}}(t) + S_{\mathbf{k}_{\rm st}}(t_0) + I_p t_0]}, \quad (23)$$

where

$$\mathbf{k}_{\rm st} = -\frac{1}{t-t_0}\int_{t_0}^{t} dt' \mathbf{A}(t') \quad (24)$$

is the stationary momentum. Introducing the travel time $\tau = t - t_0$, the integral over t_0 can be replaced by the integral over τ from $\tau = 0$ to ∞. Similarly to Eq. (20), the term $S_{\mathbf{p}}(t) + I_p t_0$ can be replaced by $\mathbf{p}\cdot\boldsymbol{\alpha}(t) + \mathcal{U}_1(t) + n\omega t - I_p\tau$. The result obtained is analogous to that of Refs. [58,64]. The double integral over t and τ can be calculated numerically. The corresponding rescattering potential and matrix elements are given in [66].

C. Saddle-point method

The integral over the direct ionization time t_0 in the T-matrix element (20) can be calculated numerically or approximately solved using the SPM. In the case of ATD by a bicircular field this has been done in Ref. [42]. In the present paper we will apply the SPM to ATI of inert atomic gases with the bound-state wave function given by Eqs. (15) and (17). The saddle-point equation is the same for ATD and ATI and is determined by the condition $d[S_{\mathbf{p}}(t_0) + I_p t_0]/dt_0 = 0$, which gives the energy-conservation condition at the ionization time t_0,

$$\tfrac{1}{2}[\mathbf{p} + \mathbf{A}(t_0)]^2 = -I_p. \quad (25)$$

The solutions of Eq. (25) for the complex time t_0 for the bicircular field were analyzed in detail in [42]. Application of the SPM in the case of the asymptotic functions (17) with $\nu = Z/\kappa = 1/\kappa \neq 0$ is more complicated [57,67]. In short, after a partial integration over the time t_0 the matrix element $\langle\mathbf{q}|V_{\rm le}(t_0)|\psi_i\rangle$, with $\mathbf{q} = \mathbf{p} + \mathbf{A}(t_0)$, is replaced by the function $-(I_p + \mathbf{q}^2/2)\tilde{\psi}_i(\mathbf{q})$, where $\tilde{\psi}_i(\mathbf{q}) = (2\pi)^{-3/2}\int d\mathbf{r}\,\psi_i(\mathbf{r})\exp(-i\mathbf{q}\cdot\mathbf{r})$ is the momentum-space asymptotic wave function, which can be expressed as a product of the Gauss hypergeometric series ${}_2F_1(a,b;c;-\mathbf{q}^2/\kappa^2)$ and the solid harmonics $Y_{lm}(\hat{\mathbf{q}})(q/\kappa)^l$. The saddle-point equation implies that $\mathbf{q}^2 = -\kappa^2$, so, with a proper choice of the integration contour in the complex plain, one obtains [3,57,67,68]

$$T^{\rm SFA,SP}_{\mathbf{p}i}(n) = i2^{-3/2}T^{-1}A\kappa^{\nu}\nu\Gamma(\nu/2) \times \sum_s \left(\frac{q_s}{i\kappa}\right)^l Y_{lm}(\hat{\mathbf{q}}_s)\left(\frac{2i}{S''_s}\right)^{(\nu+1)/2} e^{iS_s}, \quad (26)$$

where $\mathbf{q}_s = \mathbf{p} + \mathbf{A}(t_{0s})$, $S_s = S_{\mathbf{p}}(t_{0s}) + I_p t_{0s}$, and $S''_s = d^2S_s/dt_0^2 = -\mathbf{E}(t_{0s})\cdot[\mathbf{p} + \mathbf{A}(t_{0s})]$. The summation in Eq. (26) is over those complex saddle-point solutions of Eq. (25) for the ionization time t_0 that are located in the upper half of the complex t_0 plane.

The subintegral function in the five-dimensional integral that appears in the T-matrix element (22) can be presented in the form $A_{\mathbf{p}i}\exp(iS_{\mathbf{p}i})$, where

$$S_{\mathbf{p}i}(t,t_0,\mathbf{k}) = -\int_t^{\infty} dt'[\mathbf{p} + \mathbf{A}(t')]^2/2 - \int_{t_0}^{t} dt'[\mathbf{k} + \mathbf{A}(t')]^2/2 + I_p t_0 \quad (27)$$

is the action. The integral in (22) can be solved using the five-dimensional SPM. The stationarity condition for the integral over the intermediate electron momentum $\mathbf{k}$ leads to Eq. (24), which physically corresponds to the requirement that the electron returns to its parent ion. For $\mathbf{k} = \mathbf{k}_{\rm st}$ the stationarity conditions for the integral over the ionization time t_0 and the rescattering time t give

$$\tfrac{1}{2}[\mathbf{k} + \mathbf{A}(t_0)]^2 = -I_p, \quad (28)$$

$$\tfrac{1}{2}[\mathbf{k} + \mathbf{A}(t)]^2 = \tfrac{1}{2}[\mathbf{p} + \mathbf{A}(t)]^2, \quad (29)$$

which are the energy-conservation conditions at times t_0 and t, respectively. The complex solutions of the system of equations (28) and (29) for times t_0 and t, for linear polarization of the laser field, were analyzed in detail in [50–52,69]. In the present paper, we will find analogous solutions for the bicircular field.

We will first present the modified SPM, which was introduced in [70] (for HHG) and in [3] (for HATI by a few-cycle laser pulse). In the usual application of the SPM, one carries out the integral over t_0 and t in Eq. (23) using the two-dimensional SPM in which the determinant with the factor

$$\left[\left(\frac{\partial^2 S_{\mathbf{p}i}}{\partial t_0 \partial t}\right)^2 - \frac{\partial^2 S_{\mathbf{p}i}}{\partial t_0^2}\frac{\partial^2 S_{\mathbf{p}i}}{\partial t^2}\right]^{-1/2}$$

appears. In the modified SPM, one first solves the integral over t_0 similarly to how it was done for the direct SFA. Now, instead of S_s, as in Eq. (26), the action $S_{\mathbf{p}i}$ and $S''_{\mathbf{p}i0} = \partial^2 S_{\mathbf{p}i}/\partial t_0^2 = -\mathbf{E}(t_0)\cdot[\mathbf{k} + \mathbf{A}(t_0)]$ appear. After that, the SPM is applied to

the three-dimensional integral over $\mathbf{k}$ so that $\mathbf{k} \to \mathbf{k}_{\rm st}$ [Eq. (24)] and the factor $\{2\pi/[i(t-t_0)]\}^{3/2}$ appears as in Eq. (23). Then the remaining integral over t is treated with the standard one-dimensional SPM, which generates the factor $(2\pi i/S''_{\mathbf{p}i})^{1/2}$, with $S''_{\mathbf{p}i} = \partial^2 S_{\mathbf{p}i}/\partial t^2$. However, since $\mathbf{k}_{\rm st}$ depends on t one has to be careful in calculating the derivatives with respect to t. In this case, we get $S''_{\mathbf{p}i} = (\mathbf{k}_{\rm st} - \mathbf{p}) \cdot \mathbf{E}(t) + [\mathbf{k}_{\rm st} + \mathbf{A}(t)]^2/(t - t_0)$. As the final result we obtain

$$T_{\mathbf{p}i}^{\rm ISFA,SP}(n) = \pi^2 T^{-1} A \kappa^{\nu} \nu \Gamma(\nu/2) \times \sum_{\{t_{0s},t_s\}} \left(\frac{q_s}{i\kappa}\right)^l Y_{lm}(\hat{\mathbf{q}}_s) \frac{\langle \mathbf{p}|V|\mathbf{k}_{\rm st}\rangle}{[i(t_s - t_{0s})]^{3/2}} \times \left(\frac{2i}{S''_{\mathbf{p}i0,s}}\right)^{(\nu+1)/2} \left(\frac{2i}{S''_{\mathbf{p}i,s}}\right)^{1/2} e^{iS_{\mathbf{p}i,s}}, \quad (30)$$

where the sum is over the simultaneous complex solutions of the system of equations (28) and (29). Here $q_s/i\kappa$ is equal to 1 (up to a sign since $\mathbf{q}_s^2 = -\kappa^2$). In our calculations with the bicircular field we will need the spherical harmonics $Y_{00}(\hat{\mathbf{q}}) = 1/\sqrt{4\pi}$ (for He) and $Y_{1\pm1}(\hat{\mathbf{q}}) = \mp\sqrt{3/8\pi}(q_x \pm iq_y)/|\mathbf{q}|$ for all other inert gases [for $l = 1$ the term $m = 0$ does not contribute since the corresponding matrix element is zero, i.e., $\langle \mathbf{q}|\mathbf{r} \cdot \mathbf{E}(t_0)|\psi_i\rangle = 0$].

D. Definition of the bicircular field

A bicircular laser field is a superposition of two coplanar counterrotating fields having the angular frequencies $r\omega$ and $s\omega$, which are integer multiples of the same fundamental frequency $\omega = 2\pi/T$. It is defined by

$$\mathbf{E}(t) = \frac{i}{2}(E_1 \hat{\mathbf{e}}_+ e^{-ir\omega t} + E_2 \hat{\mathbf{e}}_- e^{-is\omega t}) + \text{c.c.}, \quad (31)$$

where $\hat{\mathbf{e}}_\pm = (\hat{\mathbf{e}}_x \pm i\hat{\mathbf{e}}_y)/\sqrt{2}$, with $\hat{\mathbf{e}}_x$ and $\hat{\mathbf{e}}_y$ the real unit polarization vectors along the x and y axes. In (31) E_j and $I_j = E_j^2$ are, respectively, the electric-field vector amplitude and the intensity of the jth field component with the helicities h_j ($h_1 = 1$ and $h_2 = -1$). In Fig. 1 we present the polar diagrams of the electric-field vector $\mathbf{E}(t)$, the pertinent vector potential $\mathbf{A}(t)$, and the vector $\boldsymbol{\alpha}(t)$ in the xy plane for various combinations $(r,s) = (1,2)$, $(1,3)$, $(1,4)$, and $(2,3)$. The intensities of the two components are equal. The ponderomotive energy is $U_p = U_{p1} + U_{p2} = A_1^2/4 + A_2^2/4$, with $A_1 = E_1/r\omega$ and $A_2 = E_2/s\omega$.

In principle, one can introduce arbitrary phases ϕ_1 and ϕ_2 in the definition of the bicircular field (31) by replacing $r\omega t$ with $r\omega t + \phi_1$ and $s\omega t$ with $s\omega t + \phi_2$ [71]. In this case, the field components are

$$E_x(t) = [E_1 \sin(r\omega t + \phi_1) + E_2 \sin(s\omega t + \phi_2)]/\sqrt{2},$$
$$E_y(t) = [-E_1 \cos(r\omega t + \phi_1) + E_2 \cos(s\omega t + \phi_2)]/\sqrt{2}. \quad (32)$$

A change of the phase ϕ_1, for a fixed value of ϕ_2, corresponds to a rotation of the field around the z axis by the angle $\alpha = s\phi_1/(r+s)$. Analogously, we have $\alpha = -\phi_2/(r+s)$ for a change of phase ϕ_2 (with ϕ_1 fixed). For example, for the ω-2ω field and $\phi_1 = 60^\circ$ we have $\alpha = 40^\circ$. This can be useful in experiments since it is easier to change the relative phases ϕ_1 and ϕ_2 than to rotate the detector.

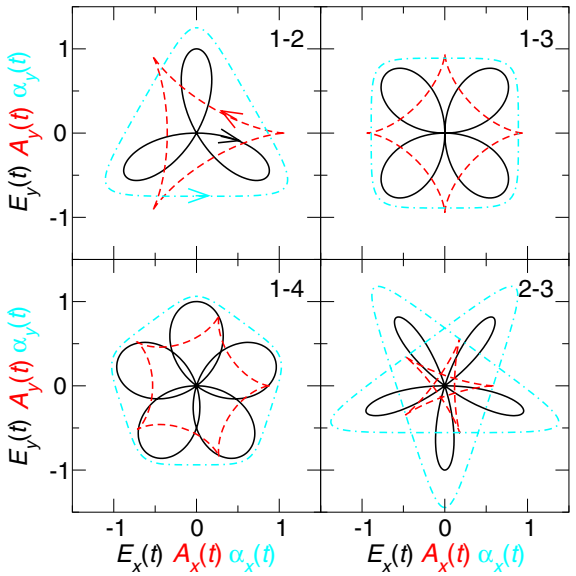

FIG. 1. Electric-field vector $\mathbf{E}(t)$, $0 \leqslant t \leqslant T$ (solid lines), and the corresponding vector potential $\mathbf{A}(t)$ [dashed (red) lines] and the vector $\boldsymbol{\alpha}(t)$ [dot-dashed (cyan) line] of the $r\omega$-$s\omega$ bicircular laser field (31). The intensities of the field components are equal and the results are presented in arbitrary units. The electric-field vector starts from the point $\mathbf{E}(0) = (0,0)$ and develops in the clockwise direction for $t > 0$, while the vector potential develops counterclockwise as indicated by the arrows in the top left panel. The various panels depict the field for different combinations of the values of r and s as indicated.

E. Classical cutoff law for a bicircular field

The so-called simple man model [72] neglects the ionization potential I_p in Eq. (25). In consequence, it has real solutions corresponding to electrons that start their orbits with zero velocity. If so, the kinetic energy of the direct electron at the detector is

$$E_{\mathbf{p}} = \mathbf{A}^2(t_0)/2. \quad (33)$$

This energy is extremal for those particular values of the ionization time t_0 for which $dE_{\mathbf{p}}/dt_0 = 0$, i.e., $\mathbf{E}(t_0) \cdot \mathbf{A}(t_0) = 0$. Then from Eq. (32) we obtain the condition $\sin[(r+s)\omega t_0 + \phi_1 + \phi_2] = 0$, so $(r+s)\omega t_0 + \phi_1 + \phi_2 = k\pi$, k is an integer, and

$$(E_{\mathbf{p}})_{\rm max,\,min} = \tfrac{1}{4}(A_1 \pm A_2)^2, \quad (34)$$

so that

$$(E_{\mathbf{p}}/U_{p1})_{\rm max,\,min} = \left(1 \pm q\frac{r}{s}\right)^2, \quad q = E_2/E_1. \quad (35)$$

The same analytical formula for the cutoff law is valid also for a corotating bicircular field. Numerical results for these cutoff laws are presented in Ref. [45]. The simple man model is very useful for an understanding of ionization by a bicircular field in so much as direct electrons are responsible [45].

F. Symmetry considerations for a bicircular field

The bicircular field (31) obeys the dynamical symmetry

$$\mathbf{E}'(t) \equiv R_z(\alpha_j)\mathbf{E}(t) = \mathbf{E}(t+\tau_j), \qquad \tau_j = jT/(r+s), \quad \alpha_j = -jr\omega\tau_j, \tag{36}$$

where j is an integer. The prime denotes the vector rotated by the 2×2 rotation matrix $R_z(\alpha_j)$ by the angle α_j about the z axis, with the diagonal matrix elements equal to $\cos\alpha_j$ and the off-diagonal elements $[R_z(\alpha_j)]_{12} = -[R_z(\alpha_j)]_{21} = \sin\alpha_j$. Physically, Eq. (36) means that a rotation by the angle α_j about the z axis is equivalent to a translation in time by τ_j. Analogous relations are valid for the vectors $\mathbf{A}(t)$ and $\boldsymbol{\alpha}(t)$.

Let us consider the matrix element

$$F_{\mathbf{p}}(t_0) = \langle \mathbf{p} + \mathbf{A}(t_0)|V_{\rm le}(t_0)|\psi_i\rangle = (2\pi)^{-3/2}\int d\mathbf{r}\, e^{-i[\mathbf{p}+\mathbf{A}(t_0)]\cdot\mathbf{r}}\mathbf{r}\cdot\mathbf{E}(t_0)\psi_{ilm}(\mathbf{r}), \tag{37}$$

which appears in both the direct and the rescattering T-matrix elements (20) and (23). Using the invariance of the scalar product with respect to rotation and the relations $d\mathbf{r} = d\mathbf{r}'$ and $\psi_{ilm}(\mathbf{r}) = \psi'_{ilm}(\mathbf{r}') = e^{-im\alpha_j}\psi_{ilm}(\mathbf{r}')$ [$\psi_{ilm}(\mathbf{r})$ is an eigenstate of the z component of the angular momentum operator L_z and $\psi' = e^{-iL_z\alpha_j}\psi$], we get

$$F_{\mathbf{p}}(t_0) = \int \frac{d\mathbf{r}'}{(2\pi)^{3/2}} e^{-i[\mathbf{p}'+\mathbf{A}(t_0+\tau_j)]\cdot\mathbf{r}'}\mathbf{r}'\cdot\mathbf{E}(t_0+\tau_j) \times e^{-im\alpha_j}\psi_{ilm}(\mathbf{r}') = e^{-im\alpha_j}F_{\mathbf{p}'}(t_0+\tau_j). \tag{38}$$

Analogously, for the other terms that appear in Eqs. (20) and (23) we obtain $S_{\mathbf{p}}(t_0) + I_p t_0 = S_{\mathbf{p}'}(t_0+\tau_j) + I_p(t_0+\tau_j) - n\omega\tau_j$ and $S_{\mathbf{p}}(t) - S_{\mathbf{k}_{\rm st}}(t) = S_{\mathbf{p}'}(t+\tau_j) - S_{\mathbf{k}'_{\rm st}}(t+\tau_j)$. Then, with the aid of the substitutions $t'_0 = t_0 + \tau_j$ and $t' = t + \tau_j$, we find

$$T^{\rm SFA}_{\mathbf{p}i}(n) + T^{\rm ISFA}_{\mathbf{p}i}(n) = e^{i\varphi}\left[T^{\rm SFA}_{\mathbf{p}'i}(n) + T^{\rm ISFA}_{\mathbf{p}'i}(n)\right], \tag{39}$$

where $\varphi = -m\alpha_j - n\omega\tau_j$. Therefore, both the direct and the rescattering T-matrix elements are invariant with respect to a rotation by the angle $\alpha_j = -2\pi jr/(r+s)$ up to the same phase factor, which confirms the corresponding $(r+s)$-fold rotational symmetry of the differential ionization rate. Actually, this rotational symmetry is observed by the exact ionization amplitude as was shown in general [42].

For the direct electrons we have additional reflection symmetries. The vector potential $\mathbf{A}(t)$ (see Fig. 1) and the direct differential ionization rate (see Fig. 2) obey reflection symmetry about the axes at the angles $\beta_j = -\alpha_j/2 = jr\pi/(r+s)$ with respect to the positive A_x and p_x axes, respectively. Since we have already proven the $(r+s)$-fold rotational symmetry of the spectrum, in order to prove the consequences of this reflection symmetry it is enough to do it for the angle $\beta_1 = \pi r/(r+s)$. Reflection about a line through the origin that makes an angle β_1 with the x axis is given by the 2×2 reflection matrix $P_x(\beta_1)$, with the off-diagonal matrix elements equal to $\sin(2\beta_1)$ and the diagonal matrix elements $[P_x(\beta_1)]_{11} = -[P_x(\beta_1)]_{22} = \cos(2\beta_1)$. It can be shown that the vectors $\mathbf{E}(t)$ and $\mathbf{A}(t)$ satisfy the relations

$$\mathbf{E}''(t) \equiv P_x(\beta_1)\mathbf{E}(t) = -\mathbf{E}(\tau_1 - t), \quad \mathbf{A}''(t) = \mathbf{A}(\tau_1 - t), \tag{40}$$

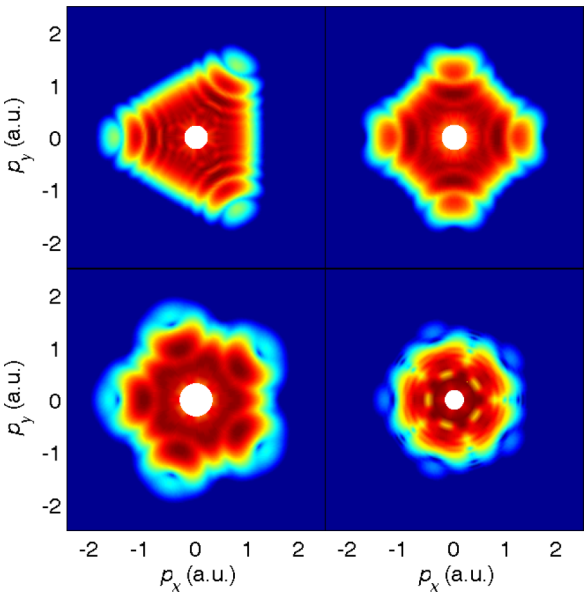

FIG. 2. Logarithm of the differential ionization rate (in a.u.) of Ne atoms presented in false colors in the electron momentum plane for ionization by a bicircular $r\omega$-$s\omega$ laser field with values of r and s as in Fig. 1, equal intensity of both components $I_1 = I_2 = 2\times 10^{14}$ W/cm^2, and the fundamental wavelength of 800 nm. The results are obtained by numerical integration of the direct SFA matrix element and using the exact wave functions. The false color scale covers four orders of magnitude.

where $\tau_1 = T/(r+s)$ and the double prime denotes the reflection defined above. This reflection matrix is composed of two rotational and one reflection matrix: $P_x(\beta_1) = R_z(\beta_1)P_x(0)R_z(\beta_1)$. Therefore, the wave function under this reflection behaves as $\psi''_{ilm} = e^{-iL_z\beta_1}\hat{P}_{yz}e^{-iL_z\beta_1}\psi_{ilm} = e^{-iL_z\beta_1}\hat{P}_{yz}e^{-im\beta_1}\psi_{ilm} = e^{-im\beta_1}e^{-iL_z\beta_1}\psi_{il,-m} = \psi_{il,-m} = (-1)^m\psi^*_{ilm}$, where we have used the fact that the reflection $x\to -x$ corresponds to the reflection about the yz plane so that the angular coordinates $(\theta,\phi)\to(\theta,\pi-\phi)$ and the spherical harmonics $Y_{lm}(\theta,\phi)\to Y_{lm}(\theta,\pi-\phi) = Y_{l,-m}(\theta,\phi) = (-1)^m[Y_{lm}(\theta,\phi)]^*$. Using the spatial inversion property of the spherical harmonics $Y_{lm}(\pi-\theta,\pi+\phi) = (-1)^l Y_{lm}(\theta,\phi)$ and having in mind that the Hamiltonian $H_0 + V$ is invariant with respect to the reflection that corresponds to $P_x(\beta_1)$, we can write

$$\psi_{ilm}(\mathbf{r}) = \psi''_{ilm}(\mathbf{r}'') = (-1)^{l+m}[\psi_{ilm}(-\mathbf{r}'')]^*. \tag{41}$$

Using Eqs. (40) and (41), it can be checked that $S_{\mathbf{p}}(t_0) + I_p t_0 = -[S_{\mathbf{p}''}(\tau_1 - t_0) + I_p(\tau_1 - t_0)] + n\omega\tau_1$ and $F_{\mathbf{p}}(t_0) = (-1)^{l+m}[F_{\mathbf{p}''}(\tau_1 - t_0)]^*$, so for the direct T-matrix element we obtain

$$T^{\rm SFA}_{\mathbf{p}i}(n) = (-1)^{l+m}e^{in\omega\tau_1}\left[T^{\rm SFA}_{\mathbf{p}''i}(n)\right]^*, \tag{42}$$

which confirms the invariance of the corresponding differential ionization rate of direct electrons with respect to the reflection $P_x(\beta_1)$. However, as soon as rescattering is involved, the fact that $t_r > t_0$ prevents one from exploiting the reflection symmetry (40), since the latter involves time inversion. Therefore, by inspecting a given (theoretical or experimental) velocity map with respect to presence or absence of the reflection

symmetries one can assess the significance of rescattering. It is important to note that Coulomb corrections act like rescattering in that they will spoil the reflection symmetry.

III. NUMERICAL RESULTS

The numerical results in this paper will be presented for ionization of Ne atoms by a bicircular $r\omega$-$s\omega$ laser field with equal intensity of both components $I_1 = I_2 = 2 \times 10^{14}$ W/cm^2 and the fundamental wavelength of 800 nm (for $r = 1$ it is $U_{p1} = 0.4392$ a.u. and $\sqrt{20U_{p1}} = 2.964$ a.u.). In addition, we will show results for ionization of Ar atoms, which were used in the experiment [43]. We will mostly investigate the ω-2ω case since it is the most interesting from the practical point of view, as mentioned in the Introduction. The special case ω-ω is equivalent to a linearly polarized field.

A. Direct SFA

The direct SFA for the case of ATD by a bicircular field was analyzed in Ref. [42]. For the $r\omega$-$s\omega$ field the parametric plot of the field is invariant with respect to rotation by the angles $2\pi j/(r+s)$, $j = 1, \ldots, r+s$. Therefore, for the $r\omega$-$s\omega$ field we observe $(r+s)$-fold rotational symmetry of the differential ionization rate. This is clearly visible in Fig. 2, where we present the results obtained using Eq. (20) (one-dimensional numerical integration over the ionization time and the bound state of the Ne atom modeled by a linear combination of four $2p$ Slater-type orbitals). The central circle in Fig. 2 is related to the minimum electron kinetic energy determined by the energy-conservation condition $E_{\mathbf{p}_{\min}} = n_{\min}\omega - I_p - U_p > 0$.

Using the SPM with the asymptotic bound state of the Ne atom and Eq. (26), we have obtained approximately the same results as those presented in Fig. 2. If we neglect the ionization potential I_p in the saddle-point equation (25), we obtain that the electrons are predominantly emitted opposite to the direction of the vector potential at the ionization time, i.e., $\mathbf{p} = -\mathbf{A}(t_0)$. According to the shape of $\mathbf{A}(t)$ for the ω-2ω case, presented in the top left panel of Fig. 1, it follows that the emission in the directions $\theta = 60^\circ$, 180°, and 300° is the dominating feature of the spectrum, which is in agreement with the result of Fig. 2. For the ω-3ω case (top right panels in Figs. 1 and 2) the relevant directions are $\theta = 0^\circ$, 90°, 180°, and 270°, while for the ω-4ω case (bottom left panels) and the 2ω-3ω case (bottom right panels) we have $\theta = 36^\circ$, 108°, 180°, 252°, and 324°.

For a complete picture we should have in mind that the solutions of Eq. (25) for $I_p \neq 0$ are complex. The number of saddle-point solutions of Eq. (25) in the upper half of the complex t_0 plane is $r + s = 3$, as was shown in [42]. In order to illustrate the SPM, in Fig. 3 we present the spectra, the saddle-point solutions, and the relevant quantum orbits, for the fixed electron emission angle $\theta = 50^\circ$ with respect to the x axis. Figure 3 consists of three panels. In the right-hand panel we compare the differential ionization rate obtained using the SPM and the asymptotic wave functions with the rate obtained by numerical integration of the direct SFA matrix element and using the exact wave functions. The agreement is very good. In the top middle panel we show the ionization time in the complex t_0 plane. There are three solutions and the electron

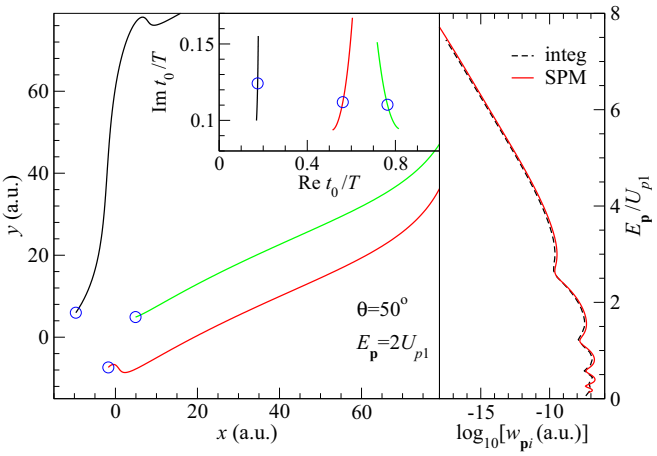

FIG. 3. Shown in the right-hand panel is a comparison of the differential ionization rate obtained by numerical integration (black dashed curve) with the rate obtained using the SPM (red solid curve), presented as a function of the electron energy $E_{\mathbf{p}}$ (in units of the ponderomotive energy of the ω field component). The top middle panel shows three complex saddle-point solutions for the ionization time t_0 (in units of the optical period T; the electron energy on each curve changes continuously from $0.2U_{p1}$ to $8U_{p1}$). The left panel shows electron trajectories for the saddle-point solutions from the top middle panel and fixed electron energy $E_{\mathbf{p}} = 2U_{p1}$. The laser and atomic parameters are as in Fig. 2 and the electron emission angle is $\theta = 50^\circ$.

energy for each solution changes continuously (towards larger values of Im t_0) from $0.2U_{p1}$ to $8U_{p1}$. The energy $E_{\mathbf{p}} = 2U_{p1}$ is indicated by a circle on each curve. For this energy we calculated the quantum orbits and show the corresponding electron trajectories depicted by curves having the same color as those for the solutions t_0 in the top panel. The quantum orbits are defined as the solutions of the classical Newton equation of motion for the electron in the presence of the laser field, $\ddot{\mathbf{r}}(t) = -\mathbf{E}(t)$, for the complex ionization time t_0, while the electron trajectories are defined as the real part of $\mathbf{r}(t)$ for $t >$ Re t_0: $\mathbf{r}(t) = (t - t_0)\mathbf{p} + \boldsymbol{\alpha}(t) - \boldsymbol{\alpha}(t_0)$. Since Re $\mathbf{r}$(Re t_0) $\neq \mathbf{0}$, the electron starts a few atomic units away from the origin (approximately at the "exit of the tunnel") and is subsequently driven by the laser field to the detector under the angle $\theta = 50^\circ$.

In the experiment [43] ionization of Ar atoms with the bicircular field with intensities $I_1 = I_2 = 5 \times 10^{13}$ W/cm^2 and a fundamental wavelength of 790 nm was considered. Since the definition of the bicircular field was different in [43], we choose $h_1 = -1$, $h_2 = 1$, $\phi_1 = 0$, and $\phi_2 = \pi$ in order to obtain agreement with the results of [43] [compare the field in the top panel of our Fig. 4 and Fig. 2(a) in [43]]. In the bottom panel of Fig. 4 we show our numerical results obtained using the SPM and the asymptotic wave function. These results agree well with the experimental results presented in Fig. 3(c) in [43].

B. Rescattering ISFA: Numerical integration

In Fig. 5 we show the differential ionization rates obtained by two-dimensional numerical integration (23). From the top left panel it is obvious that the threefold rotational symmetry of the ionization spectrum generated by the bicircular ω-2ω

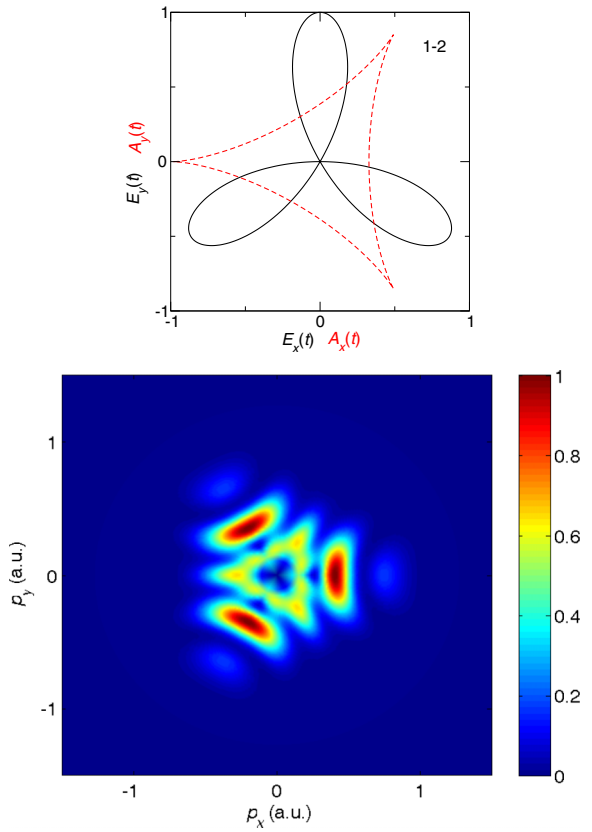

FIG. 4. Differential ionization rate of Ar atoms presented in false colors in the electron momentum plane for ionization by a bicircular ω-2ω laser field with equal intensity of both components $I_1 = I_2 = 5 \times 10^{13}$ W/cm^2, the fundamental wavelength of 790 nm, $h_1 = -1$, $h_2 = 1$, $\phi_1 = 0$, and $\phi_2 = \pi$. The results are obtained using the SPM with the asymptotic wave function. The false color scale is linear and normalized to 1. The corresponding bicircular field and vector potential, in arbitrary units and normalized to one, are shown in the top panel.

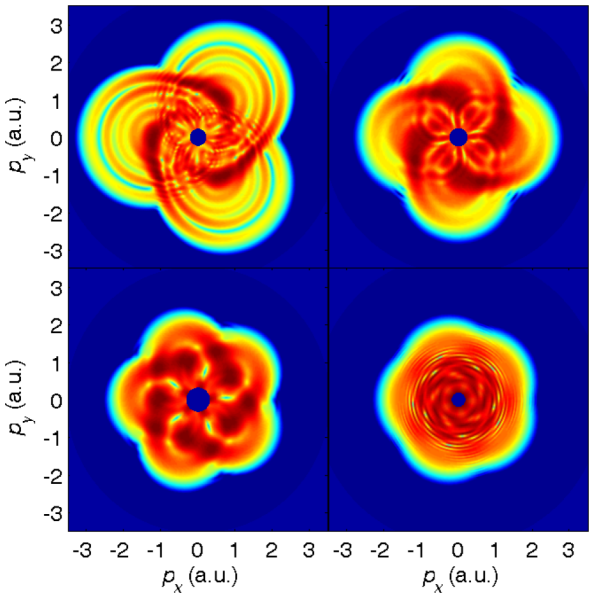

FIG. 5. Logarithm of the differential ionization rate for the same parameters as in Fig. 2 and presented similarly. The ISFA result (23) is obtained by two-dimensional numerical integration and using four $2p$ Slater-type orbitals (16) to represent the ground state of the Ne atom.

field is valid also for the rescattered electrons. The electron energies can be larger than $10U_{p1}$. The spectrum looks like a superposition of the three spectra generated by three linearly polarized laser fields rotated by the angle 120° with respect to the other. Let us briefly recall the HATI spectrum presented in the form of a velocity map generated by one linearly polarized laser field: It follows the shape of concentric circles with centers at $\pm E_0/\omega$, where E_0 is the electric-field vector amplitude. More precisely, these circles are more like droplets (see Fig. 3 in [49] and Fig. 3 in [50]). The HATI spectra for the linearly polarized field case were explained in detail in Refs. [49–53] in terms of backward- and forward-scattered electrons. Backscattering is responsible for the high-energy electrons, which have a cutoff at the energy $10U_{p\mathrm{lin}}$, with the corresponding ponderomotive energy $U_{p\mathrm{lin}} = E_0^2/4\omega^2$. The forward-scattered electrons are responsible for the LES and the off-axis LES (for details see Refs. [49–54]). Returning to the ω-2ω bicircular case, the top left panel of Fig. 5 exhibits three such structures as just described. In addition to the concentric circles or dropletlike-shape structures, which reach energies up to $10U_{p1}$, we observe enhancements of the central parts of each structure situated near the angles 50°, 170°, and 290°.

In the remaining panels of Fig. 5 we show the spectra for the ω-3ω (top right panel), ω-4ω (bottom left panel), and 2ω-3ω (bottom right panel) fields. The results are qualitatively similar to those of the ω-2ω case, except that they exhibit an $(r+s)$-fold, instead of the threefold, rotational symmetry. Note that the velocity maps of Fig. 5 violate the reflection symmetries (40), since in contrast to those in Figs. 2 and 4 they do include rescattering.

IV. QUANTUM-ORBIT ANALYSIS OF THE ISFA RESULTS

In this section we will analyze the saddle-point solutions of Eqs. (28) and (29) and the corresponding quantum orbits, which are relevant for the rescattered electrons. In our previous work [52] we introduced a classification of the saddle-point solutions for HATI by a linearly polarized field. Namely, we restricted the real part of the rescattering time t_r to within one cycle of the field so that $0 \leqslant \mathrm{Re}\, t_r < T$ and determined the solutions $\{t_0, t_r\}$ such that $\mathrm{Re}\, t_0 < \mathrm{Re}\, t_r$ [positive travel time $\mathrm{Re}\,(t_r - t_0)$]. The solutions were divided into two groups: The backward-scattering solutions were classified by the multiple index (α,β,m), while for the forward-scattering solutions the double index (ν,μ) was used.

A. High-energy rescattering

In this subsection we consider only the backward-scattering solutions (α,β,m) since they are relevant for the high-energy electrons. Physically, the index m gives the approximate length of the travel time in multiples of the laser period. Solutions usually come in pairs. For fixed m, the index β enumerates different pairs of solutions within one optical cycle. Finally,

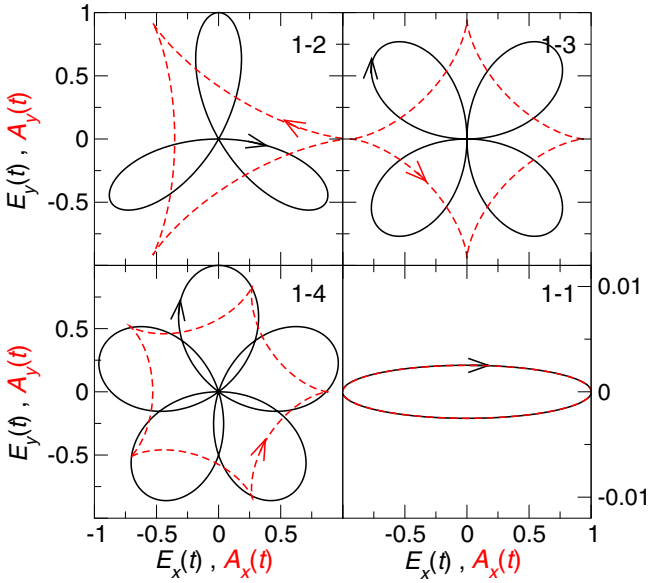

FIG. 6. Electric-field vector $\mathbf{E}(t), 0 \leqslant t \leqslant T$ (solid lines), and the corresponding vector potential $\mathbf{A}(t)$ [dashed (red) lines] of the $r\omega$-$s\omega$ bicircular laser field (31), presented similarly to Fig. 1. For the 1-1 case a small ellipticity is introduced ($\varepsilon_1 = 0.99$) in order to visually distinguish the field in the direction of the x axis and in the opposite direction (notice the different scale of the y axis for the bottom right panel).

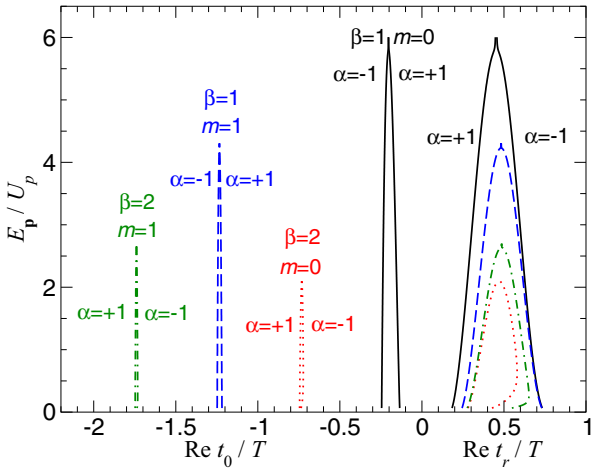

FIG. 7. Examples of the notation (α,β,m) used to label the solutions of the system of the saddle-point equations (28) and (29) for linear polarization (which is equivalent with the ω-ω bicircular field). The solid, dotted, long-dashed, and dot-dashed curves in the right-hand part ($t > 0$) of the figure ($0 \leqslant \mathrm{Re}\, t_r \leqslant T$) specify the real part of the rescattering times for the four pairs of orbits with the shortest travel times. In the left-hand part of the figure ($t < 0$), the counterpart of each curve identifies the corresponding real part of the ionization times t_0. The emitted electron energy in multiples of U_p is plotted on the ordinate. Horizontal lines at constant energy (not shown) relate the real parts of the ionization and rescattering times for the respective orbits. There are infinitely many further solutions that have their real parts of the ionization time beyond the left-hand margin of the figure. The curves have been calculated for Ne, for emission in the direction $\theta = 50^\circ$ (rather than 0°, which is why the maximal energy is lower than $10U_p$), and for a laser field having the intensity 2×10^{14} W/cm^2 and the fundamental wavelength of 800 nm.

for fixed β and m, each pair of solutions consists of two orbits with slightly different travel times and we discriminate the longer ($\alpha = -1$) from the shorter orbit ($\alpha = +1$) by the index α (the terminology "short" and "long" orbits derives from the Lewenstein model [73] of HHG where only the shortest pair of solutions is considered).

The classification (α,β,m), which was introduced for linear polarization, applies for the bicircular field as well [74]. In order to explain this we use Fig. 6, where the bottom right panel shows a linearly polarized field vector that changes along the x axis (a small nonzero ellipticity is introduced in order to make it easier to follow the change of the field with time). Within one optical cycle T, the field traces out two segments of the x axis in opposite directions (0° and 180°). These two segments are completely analogous to the three segments for the angles 0°, 120°, and 240°, which we have for the ω-2ω bicircular field shown in the top left panel. For the ω-3ω case (top right panel) we have four such segments for the angles 0°, 90°, 180°, and 270°, and so on. For the $r\omega$-$s\omega$ field we have $r + s$ segments within one cycle. Therefore, in the general case, we use the index $m = 0,1,2,\ldots$ to count the approximate length of the travel time $\mathrm{Re}\,(t_r - t_0)$ in multiples of the laser period T and the index $\beta = 1,2,\ldots,r+s$ to count the segments within one optical cycle characterized by the index m. The travel time increases with the increase of the value of β. The index α again distinguishes the long from the short orbit.

In order to acquire some practice with this classification, in Fig. 7 we consider the saddle-point solutions for the simplest case ω-ω, which is equivalent with linear polarization [74]. We consider a field polarized along the x axis, $E_x(t) = E_0 \sin(\omega t)$, and fix the angle θ of the emitted electron with respect to the x axis. Ionization is more probable when the absolute value of the field is close to one of its maxima. For $m = 0$, i.e., for ionization within the interval $-T < \mathrm{Re}\, t_0 < 0$, there are two maxima, at $\mathrm{Re}\, t_0 = -0.75T$ and at $\mathrm{Re}\, t_0 = -0.25T$, which correspond, respectively, to the pairs of solutions $\beta = 2$ and $\beta = 1$. From Fig. 7 one can read off the ionization and rescattering times of the long and the short orbits $\alpha = -1$ and $\alpha = 1$ by drawing a horizontal line at the respective energy $E_{\mathbf{p}}$. The situation is identical for the solutions with $m = 1, 2, \ldots$.

In Fig. 8 we present the saddle-point solutions $\{t_0,t_r\}$, obtained solving the system of equations (28) and (29) using the subroutine ZSPOW from the International Mathematics and Statistics Library routines, for the ω-2ω case, classified in accordance with the notation (α,β,m) introduced above, for the parameters of Fig. 7. The only difference from linear polarization (or the ω-ω case) is that the index β now runs from 1 to 3, corresponding to the three segments of the ω-2ω field, $\alpha = \pm 1$, $\beta = 1,2,3$, $m = 0,1,2,\ldots$. Similarly to the case of a linearly polarized field, all solutions (α,β,m) [75] have a fairly well defined cutoff, which is located at the energy where the corresponding solutions with $\alpha = +1$ and -1 approach each other. From the top panel of Fig. 8 it is evident that in each optical cycle (numbered by $m = 0,1,2,\ldots$) we have $r + s = 3$ pairs of solutions, which are distinguished by the index $\beta = 1,2,3$. The members of each pair are characterized

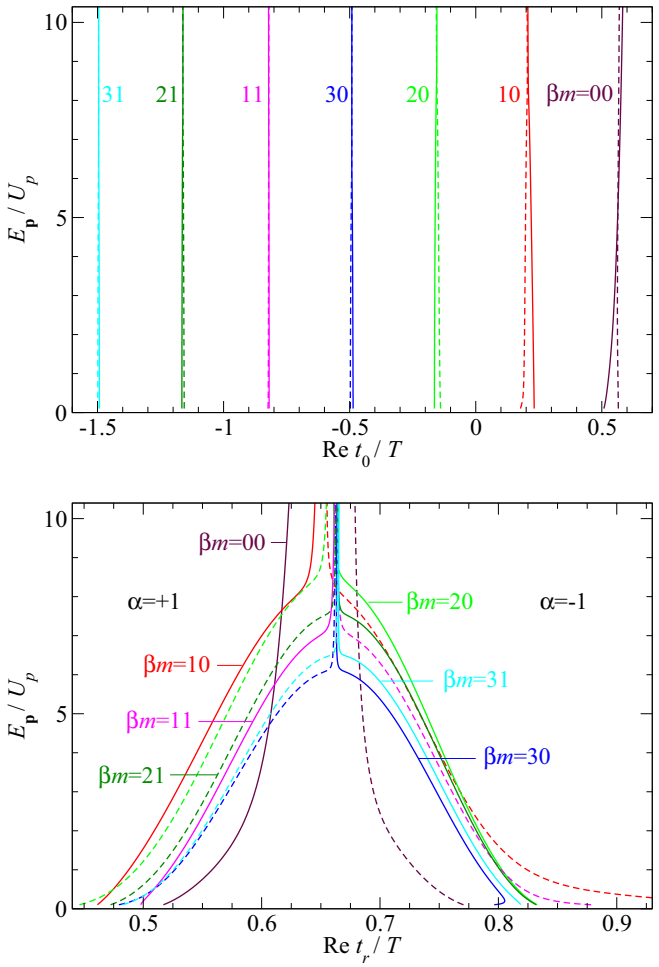

FIG. 8. Solutions of the system of the saddle-point equations (28) and (29) for the parameters of Fig. 7 and for the fixed electron emission angle $\theta = 50°$. For each of the presented solutions the electron energy $E_{\mathbf{p}}$ (in units of the ponderomotive energy U_p) is presented as a function of the real part of the electron ionization time Re t_0 (top) and rescattering time Re t_r (bottom), in units of the optical period T. The solutions whose contribution should be discarded after the cutoff are represented by the dashed lines. Each solution is denoted by the corresponding index (β,m). In the bottom panel all solutions on the left (right) have the index $\alpha = +1$ ($\alpha = -1$). There are infinitely many further solutions that have Re t_0/T beyond the left margin of the top panel.

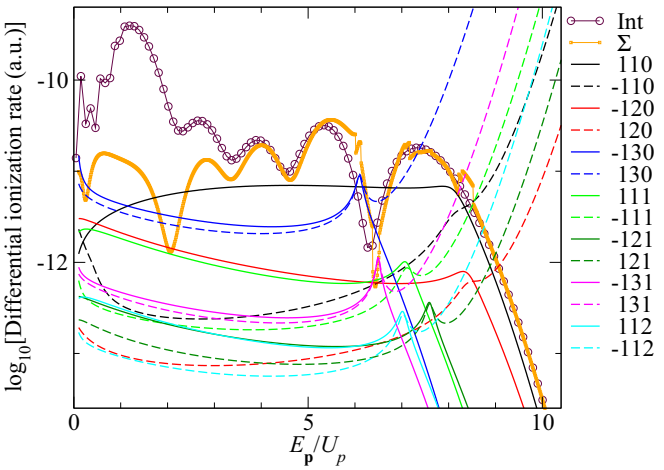

FIG. 9. Comparison of the differential ionization rates as a function of the electron energy (in units of the ponderomotive energy) for the same parameters as in Fig. 8. The results obtained by numerical integration are represented by black solid lines with circles, while the results obtained as a coherent sum of the contributions of 14 saddle-point solutions are shown by the solid orange line with squares. The contributions of the divergent solutions are neglected after the corresponding cutoff values. The partial rates for each of the 14 solutions (α,β,m) are presented and identified by their colors, as explained in the right margin.

by the index $\alpha = \pm 1$. Comparing Figs. 7 and 8, one should notice that in the former the two solutions $\alpha = \pm 1$ have only been drawn up to the energy where they have practically merged, while in the latter they are drawn all the way up to the highest energy.

As already mentioned, in this subsection we will concentrate on the solutions that contribute to the high-energy electrons [75]. We will use these solutions to calculate the differential ionization rate applying Eq. (30). Let us consider the ω-2ω case in detail. In Fig. 9 we present the rate obtained by numerical integration (23) with the rate obtained using Eq. (30) taking into account the T-matrix element for the coherent sum of 14 solutions (α,β,m), as identified in the margin of the figure. This can be compared with the individual contributions of these 14 solutions. Of each pair $(\alpha = \pm 1,\beta,m)$, one of the two solutions ($\alpha = +1$ or -1) has to be discarded for energies higher than the respective cutoff. This solution is drawn as a dashed line. We notice a relatively good agreement of the results obtained by numerical integration with those obtained using the SPM for energies above $3.2U_p$ (below this energy the contribution of the direct electrons dominates the spectrum). A small disagreement, in the form of spikes, can be noticed for those energies that correspond to the cutoffs of particular pairs of the saddle-point solutions. This is well known from the application of the SPM to HATI by a linearly polarized laser field: The SPM fails at the cutoff energies and the uniform approximation should be used instead [69,76]. Figure 9 also demonstrates the quantitative significance of the various contributing orbits. We see that throughout the plateau the orbit (1,1,0) is dominant and the two orbits ($\pm$1,3,0) are the next important ones. Their contributions are smaller by a factor of 3 or 4, except near their cutoff above $6U_p$ where their magnitude is the same as that of (1,1,0). However, due to interference an orbit may make a larger contribution than its magnitude suggests (for example, the very pronounced dip in the spectrum around $6.4U_p$ is likely due to the destructive interference of the aforementioned orbits). All the other orbits contribute only insignificantly.

We have also explored saddle-point solutions for angles θ different from 50°. For high-energy electrons the results obtained are in agreement with those in Fig. 5, which were obtained by numerical integration. As an example, in Fig. 10 we show the electron spectra for the case where the T-matrix element is obtained as the coherent sum of the two shortest quantum orbits that contribute to the high-energy electrons, i.e., the orbits $(\alpha,\beta,m) = (\pm 1,1,0)$. The spectrum is calculated

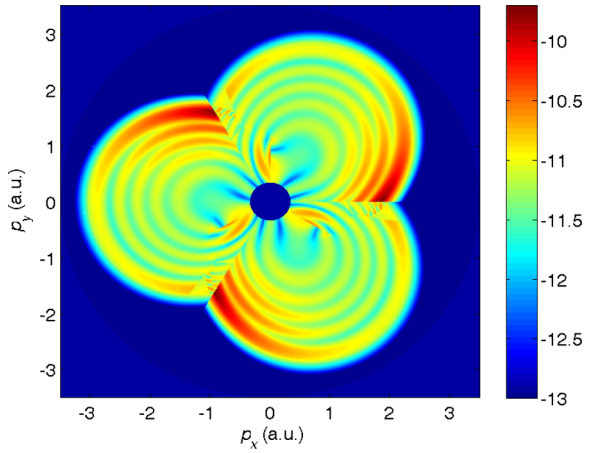

FIG. 10. Logarithm of the differential ionization rate (in a.u.) of Ne atoms represented in false colors in the electron momentum plane for ionization by a bicircular ω-2ω field. The results are obtained using the SPM with the solutions $(\alpha,\beta,m) = (\pm1,1,0)$, as explained in the text.

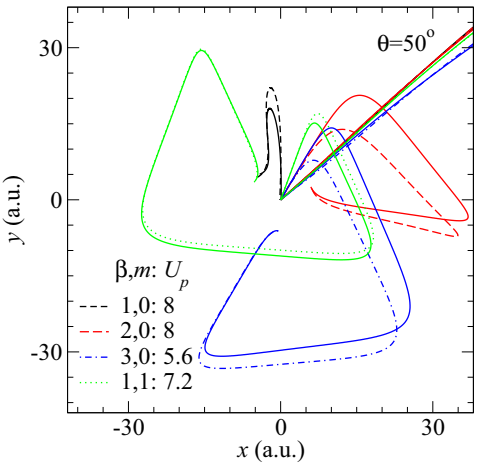

FIG. 11. Electron trajectories for some of the quantum-orbit solutions presented in Fig. 8. The electron energies for the presented pairs $\alpha = \pm1$ of solutions are $8U_p$ for the solutions $(\beta,m) = (1,0)$ and $(2,0)$, $5.6U_p$ for the solutions $(3,0)$, and $7.2U_p$ for the solutions $(1,1)$.

for $\theta \in [0^\circ,120^\circ]$ and extrapolated to all angles. Reviewing Figs. 5 and 10, we notice good qualitative agreement in those regions where the backward-scattering orbits are dominant. This way, by selecting the contribution of individual orbits and comparing with the total (theoretical or experimental) result, one can infer which orbit is responsible for a particular region of final momenta.

In order better to understand rescattering ATI induced by the bicircular-laser field, we will use the concept of quantum orbits [3,15,16,19–23,52]. These are defined as solutions of the classical Newton equation for the electron in the presence of the laser field, $\ddot{\mathbf{r}}(t) = -\mathbf{E}(t)$, but for complex ionization time t_0 and rescattering time t_r as they result from the solution of the saddle-point equations (28) and (29). For these complex times we have $\mathbf{r}(t_0) = \mathbf{r}(t_r) = \mathbf{0}$. We will define the electron trajectories as the real part of $\mathbf{r}(t)$ for t real, with

$$\mathbf{r}(t) = \begin{cases} (t-t_0)\mathbf{k}_{\rm st} + \boldsymbol{\alpha}(t) - \boldsymbol{\alpha}(t_0) & \text{for } \mathrm{Re}\, t_0 \leqslant t \leqslant \mathrm{Re}\, t_r \\ (t-t_r)\mathbf{p} + \boldsymbol{\alpha}(t) - \boldsymbol{\alpha}(t_r) & \text{for } t > \mathrm{Re}\, t_r. \end{cases} \tag{43}$$

Since $\mathrm{Re}\,\mathbf{r}(\mathrm{Re}\, t_0) \neq \mathbf{0}$, the liberated electron appears in the continuum at the exit of the tunnel, a few atomic units away from the origin. Eight typical electron trajectories that correspond to the parameters of Figs. 8 and 9 are shown in Fig. 11. The results are shown for four pairs (solid lines and the corresponding dashed, long-dashed, dot-dashed, and dotted lines) of solutions, which are numbered as in Figs. 8 and 9, and for the corresponding cutoff energies [$8U_p$, $8U_p$, $5.6U_p$, and $7.2U_p$ for the solutions $(\beta,m) = (1,0)$, $(2,0)$, $(3,0)$, and $(1,1)$, respectively]. Along the shortest trajectory (black lines) the electron moves away from the origin in the direction of the y axis and, after the field component has changed its sign, moves back to the origin, following almost the same trajectory. It was found in Ref. [27] that similar trajectories are responsible for emission of the high-energy photon in the HHG process where the returning electron recombines with its parent ion. In the present case, instead of recombining, the electron elastically scatters off the nucleus and moves in the direction $\theta = 50^\circ$ with respect to the x axis. Figure 11 also displays longer and more complicated trajectories though their contributions are smaller, as can be inferred from Fig. 9. Analogous trajectories also exist for HHG [27].

The bicircular field $\mathbf{E}(t)$ and the vectors $\mathbf{A}(t)$ and $\boldsymbol{\alpha}(t)$, as well as their values at the ionization and rescattering times, are exhibited in Fig. 12 for the parameters of Fig. 11 and the solutions presented by the solid lines. Analyzing Figs. 11 and 12, one can follow each of the quantum orbits, which contribute to the HATI process, in detail. For example, it is obvious that for all cases the field is close to its maximum at the ionization time, while the vector potential at the rescattering time is also maximal but points in the direction opposite to the emission angle $\theta = 50^\circ$.

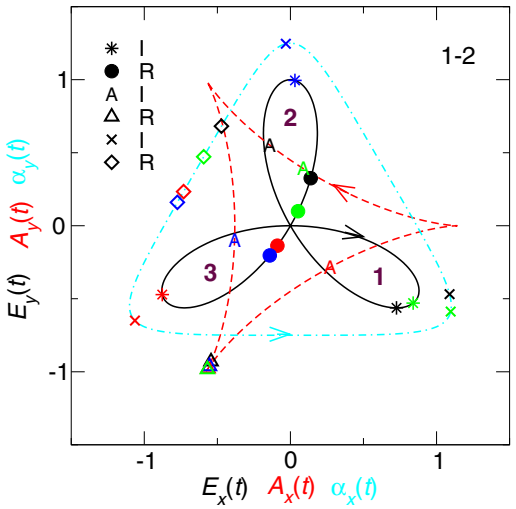

FIG. 12. Electric-field vector $\mathbf{E}(t)$ and the corresponding vectors $\mathbf{A}(t)$ and $\boldsymbol{\alpha}(t)$ of the ω-2ω bicircular laser field (31), presented as in Fig. 1. The field vectors at the ionization times (I) and rescattering times (R), for the electron trajectories that are represented by the solid lines in Fig. 11, are indicated by the symbols in the legend.

B. Physical considerations of the high-energy quantum orbits for the ω-2ω bicircular field

Here we will look at some of the orbits for the ω-2ω bicircular field in more detail. We start with backscattering into high energy (greater than $4U_p$) and will make use of the results displayed in Figs. 8–12.

The electric field (31) consists of three segments per cycle. It is defined such that at $t = 0$ the field $\mathbf{E}(0)$ points in the positive x direction. For the ω-2ω case, which is illustrated in Fig. 12, we denote the three lobes for $0 < t < T/3$, $T/3 < t < 2T/3$, and $2T/3 < t < T$, which extend, respectively, into the lower right, upward, and the lower left, by lobe 1, lobe 2, and lobe 3. Note that the electron charge is negative. Hence, the force on the electron is opposite to the field. The tunnel exit is in the direction of $-\mathbf{E}(t_0)$ if the electron exits into the continuum at the time t_0. If the electron enters the continuum around the maxima of the field, we can from Fig. 11 roughly read off the ionization times of the various orbits by locating the positions where they start (this is analogous to reading the attoclock [77]). We will focus on the orbits $(\beta,m) = (1,0)$ and $(\beta,m) = (3,0)$, which start opposite lobe 1 and lobe 2, respectively, each at a distance of about 5 a.u. off the origin. Since the electron starts its orbit with a substantially nonzero momentum, its initial trajectory is not exactly in the direction of $-\mathbf{E}(t_0)$.

We concentrate on the orbits (1,0) and (3,0), because according to Fig. 9 these are most important at high energy. In particular, the very pronounced dip in the spectrum is likely to be due to the interference of these orbits. The (1,0) orbit in Fig. 12 looks close to an orbit typical of linear polarization: It unfolds mostly in the y direction. Figure 12 shows that its electron is liberated in lobe 1 right after the field has become maximal and rescatters in lobe 2 shortly before a zero of the field. This means that in the y direction the electron is first accelerated to positive momenta and then decelerated and bent around such that it recollides with substantial momentum. The force exerted in the negative x direction mostly by the field during lobe 1 is largely compensated by the initial momentum in this direction. All this is rather parallel to orbits in a linearly polarized field. The trajectory and the velocity for the orbit $(\alpha,\beta,m) = (1,1,0)$ are illustrated in more detail separately in Fig. 13. Note that at the rescattering time the magnitude of the vector potential is practically maximal while the field is not far from zero.

The orbit (3,0) is more complicated. According to Figs. 8(a) and 8(b) its length in time is almost four-thirds of a period; so it experiences all segments of the field. Figure 12 shows that it starts almost at the maximum of the field in segment 2; so it exits the tunnel almost exactly on the negative y axis with some negative initial momentum in the x direction. Figure 12 then illustrates the action of the electric field of half the segment 2 and subsequently the full segments 3, 1, and 2, before it rescatters shortly after a zero of the field in the beginning of segment 3. The resulting orbit is approximately triangular. Its three rather straight sections are due to the action of the field in the half segment 2 and thereafter segments 3, 1, and 2.

All orbits presented in Fig. 12 rescatter into the same direction, at an angle of 50°, and the associated drift momenta are $-\mathbf{A}(t_r)$. The return times t_r are different for different orbits, approximately $t_r = 0.625T$ for the (1,0) orbit at $8U_p$ and $t_r = 0.69T$ for the (3,0) orbit at $5.6U_p$. However, the red dashed curve in Fig. 12 shows that the corresponding vector potentials are very close. The situation is then rather similar to linear polarization where the velocity map of the rescattered electrons is shaped by circles about the vector potentials $-\mathbf{A}(t_r)$ with radii that are specified by the energy of the respective recolliding electron. The bicircular field (31) generates three such groups of almost concentric circles as illustrated in Figs. 5 and 10.

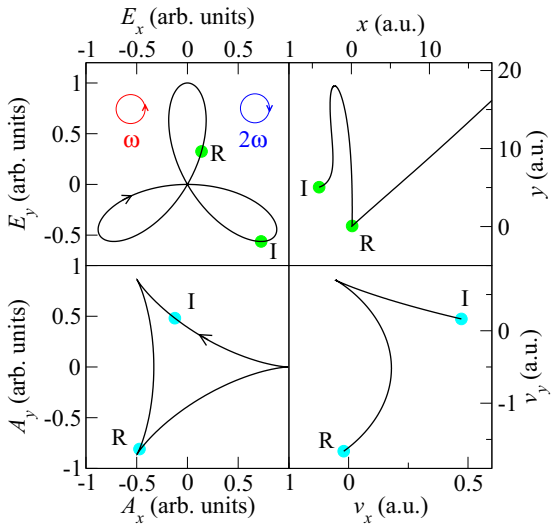

FIG. 13. The ω-2ω bicircular electric-field vector (top left), vector potential (bottom left), electron trajectory (top right), and velocity (bottom right) between the ionization times (I) and rescattering times (R) that correspond to the orbit $(\alpha,\beta,m) = (1,1,0)$ and the energy $8U_p$.

C. Low-energy rescattering

Let us now consider saddle-point solutions that contribute to the low-energy electrons for the ω-2ω field. In Fig. 14 we show various partial contributions to the ionization rate for energies lower than $3.2U_p$.

1. Backward-scattering-like solutions

We will first consider the contribution of the pair of solutions $(\alpha,\beta,m) = (\pm1,0,0)$. As we have mentioned [75], these solutions are analogous to the solution $(\alpha,\beta,m) = (\pm1,1,0)$ for the linearly polarized field case (see Figs. 9 and 10 in Ref. [52]). In Fig. 14 these solutions are represented by the red lines. The contribution of the dashed line $(-1,0,0)$ should be discarded for energies higher than some critical energy, while the contribution of the solid line (1,0,0) is relatively small. In Fig. 15 we show the corresponding saddle-point solutions in the complex time plane. We see that these solutions are strikingly similar to the solutions presented in Fig. 9 in Ref. [52]. This indicates that the short-travel-time solutions are generally very similar and are qualitatively different from the other (α,β,m) solutions. For example, as a function of the energy the time t_0 for the solution $(-1,0,0)$ forms a loop in the complex plane (bottom left panel in Fig. 15). For higher energies the contribution of this solution to the ionization rate

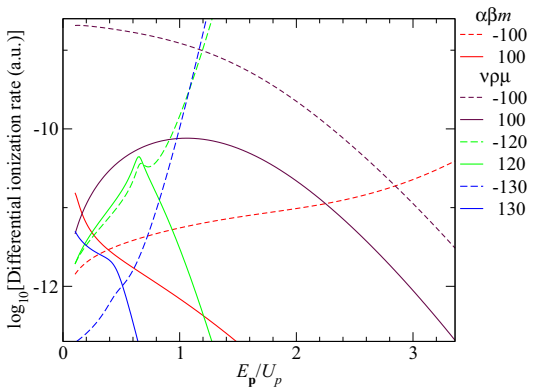

FIG. 14. Comparison of the differential ionization rates as a function of the electron energy, presented similarly to Fig. 9, but for different saddle-point solutions, as denoted in the legend. See the text for further explanation.

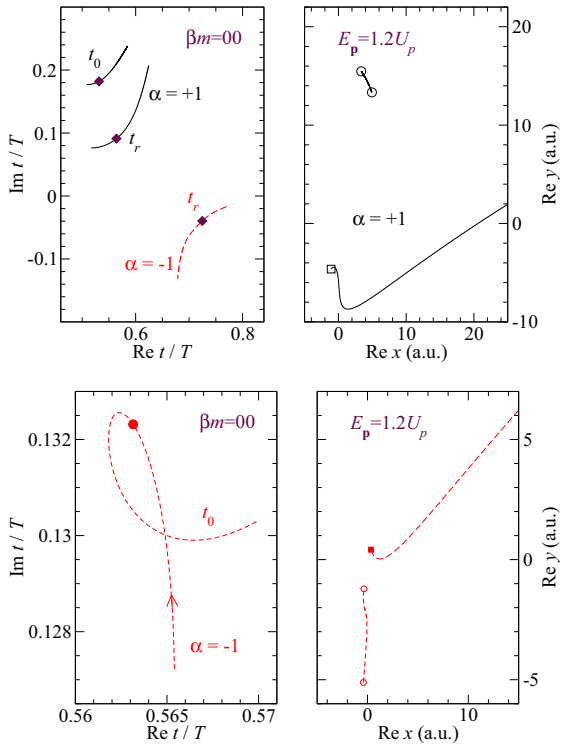

FIG. 15. Quantum-orbit solutions and trajectories for the same parameters as in Fig. 8. The left-hand panels shows the $(\alpha,\beta,m) = (\pm1,0,0)$ saddle-point solutions for the complex ionization time t_0 and rescattering time t_r. The $\alpha = -1$ ($\alpha = +1$) solutions are denoted by the red dashed (black solid) lines. The electron energy changes from a minimum value to the cutoff value as a continuous parameter along each curve. The complex time t_r of the solution $(-1,0,0)$ (red dashed line) is presented in the top left panel, while the corresponding time t_0 is shown in the bottom left panel. The complex time that corresponds to the electron energy $E_\mathbf{p} = 1.2U_p$ is denoted by diamonds (circle) in the top (bottom) left panel. The right-hand panels show electron trajectories obtained using the saddle-point solutions of the left-hand panels. The electron energy is $E_\mathbf{p} = 1.2U_p$. The exit of the tunnel and the rescattering point are denoted by the corresponding symbols. The electron leaves in the direction $\theta = 50^\circ$.

becomes divergent, but it is not easy to determine the energy after which this solution should be neglected [52]. The corresponding trajectories have a discontinuity at the rescattering time. This is a consequence of the large imaginary parts of the complex times and is particularly pronounced for the (1,0,0) solution (top right panel). A more appropriate analysis can be done using the complex-time quantum orbits [52], but we will not proceed with this in the present paper.

2. *Forward-scattering-like solutions*

For linear polarization, electrons returning with low energy and especially their forward scattering are known to be responsible for the low-energy structure and the associated off-axis effects (the soft-recollision model [78]). In Ref. [51] this was put in the context of the simple man model [72]. Namely, the condition of the electron return $x(t_r) = 0$ (for the field linearly polarized along the x axis and for the real time) is rewritten as $\alpha_x(t_r) = \alpha_x(t_0) + (t_r - t_0)\alpha_x'(t_0)$, so, for a given t_0, one can determine t_r by intersecting the curve $\alpha_x(t)$ with its tangent at t_0. In addition, for the soft-recollision model one has the condition $\dot{x}(t_r) = 0$. Taking into account that in the simple man model we also have $\dot{x}(t_0) = 0$, we obtain the condition $\alpha_x'(t_r) = \alpha_x'(t_0)$. Graphically, these times t_0 and t_r are found by determining straight lines that are tangent to $\alpha_x(t)$ at both t_0 and t_r. For fixed t_r this can happen for $-\mu < \mathrm{Re}\, t_0/T < -\mu + 1$, $\mu = 0,1,2,\ldots$, which explains the meaning of the index μ. In fact, in Ref. [51] the double index (ν,μ) was introduced to characterize the forward-scattering saddle-point solutions. The role of the index ν is similar to that of the index α: It discriminates the longer ($\nu = +1$) and the shorter ($\nu = -1$) orbits. However, the bicircular field develops in a plane and the above analysis is not directly applicable. Nevertheless, we will show that there is an analogy between the $(\nu,\mu) = (\pm1,0)$ solutions for linear polarization and particular saddle-point solutions for the bicircular field for which the travel time is short.

We denote the forward-scattering-like saddle-point solutions for the bicircular field by the multiple index (ν,ρ,μ).

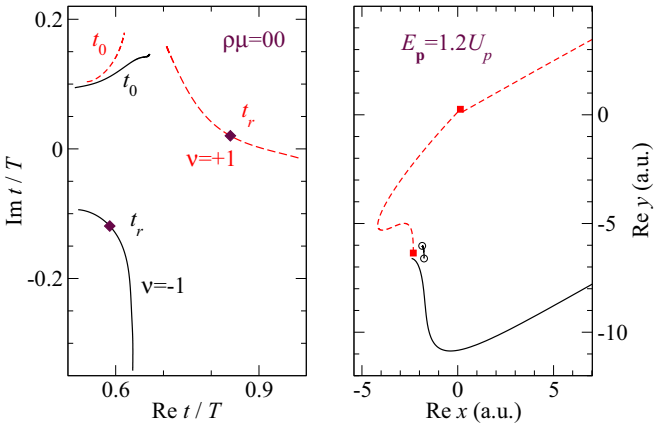

FIG. 16. Quantum-orbit solutions $(\nu,\rho,\mu) = (\pm1,0,0)$ (left) and the corresponding trajectories for the electron energy $E_\mathbf{p} = 1.2U_p$ (right) for the same parameters as in Fig. 8 and presented similarly to Fig. 15. The rescattering times that correspond to the energy $E_\mathbf{p} = 1.2U_p$ are denoted by diamonds in the left-hand panel.

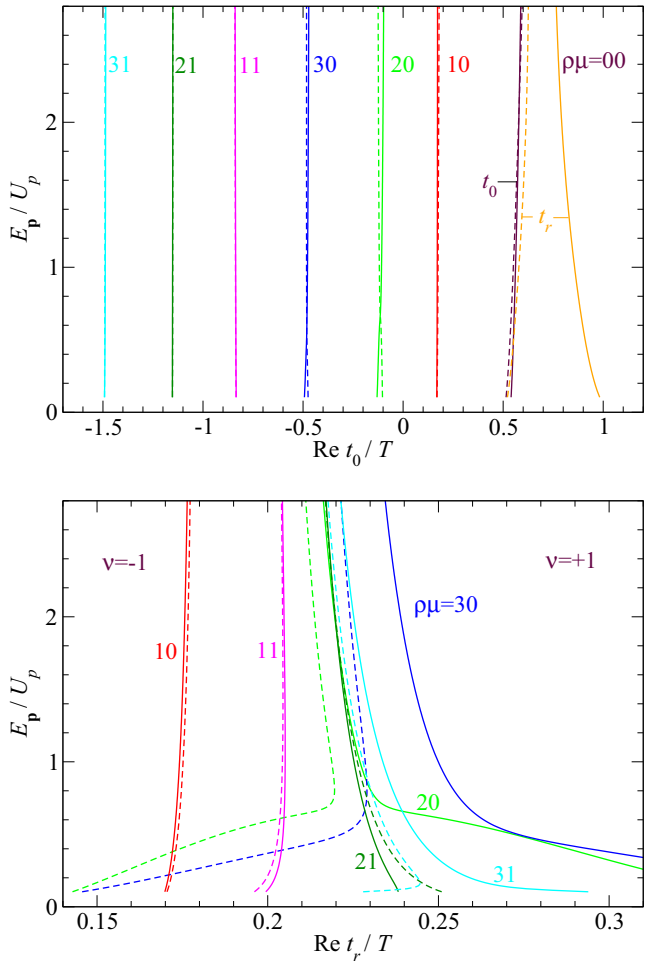

FIG. 17. Same as in Fig. 8 but for the forward-scattering-like saddle-point solutions characterized by the multiple index (ν,ρ,μ).

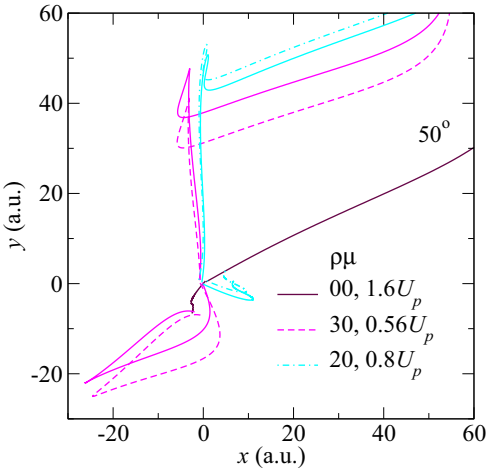

FIG. 18. Electron trajectories for five short forward-scattering-like quantum orbits and the energies as denoted in the legend. Laser and atomic parameters are as in the previous figures.

The role of the indices ν and μ is similar to the case of linear polarization, while the index ρ enumerates the solutions within one cycle, similarly to the index β for the backward-scattering-like saddle-point solutions. The most pronounced partial contributions to the ionization rate come from the solutions denoted by $(\nu,\rho,\mu) = (\pm1,0,0)$ in Fig. 14. Let us analyze the corresponding saddle-point solutions. They are presented in the left panel of Fig. 16. One can see that for the solution $(-1,0,0)$ the rescattering time is in the lower half complex time plane. Its contribution to the ionization rate should be discarded, similarly to how it was done in Ref. [52]. In fact, these solutions are the analogs of the forward-scattering solutions $(\nu,\mu) = (\pm1,0)$ for the linearly-polarized-field case from [52]. The difference is that in the present case the time t_0 is different for the solutions $\nu = \pm1$, while in [52] the time t_0 was identical for both solutions for the chosen angle $\theta = 0°$. The fact that the index ν discriminates shorter and longer orbits can be clearly seen in Fig. 16. For the solution $\nu = -1$ the electron trajectory between the ionization and rescattering time in the right-hand panel of Fig. 16 is very short (the black solid line; the contribution of this solution to the ionization rate should be dropped). However, the red dashed line (the $\nu = +1$ solution) exhibits almost forward scattering. This is the reason why the contribution of this solution is important. Furthermore, Coulomb effects further enhance the contribution of this solution. It is responsible for the experimentally observed rescattered electrons in Ref. [43].

In Fig. 17, in addition to the solutions $(\nu,\rho,\mu) = (\pm1,0,0)$ [orange and maroon lines in the top panel: $\nu = 1$ (solid lines) and $\nu = -1$ (dashed lines)], we present the saddle-point solutions (ν,ρ,μ) for $\nu = \pm1$, $\rho = 1,2,3$, and $\mu = 0,1$. From the presented solutions, for the angle $\theta = 50°$, the most important ones are those shown in Fig. 14. The contributions of the solutions presented by the dashed line should be dropped after their cutoff (for $\rho = 2,3$) or completely (for $\rho = 0$). From Fig. 14 we see that this cutoff is slightly below $0.8U_p$ for the solutions $(\pm1,2,0)$ (green curves) and $0.56U_p$ for the solutions $(\pm1,3,0)$ (blue curves).

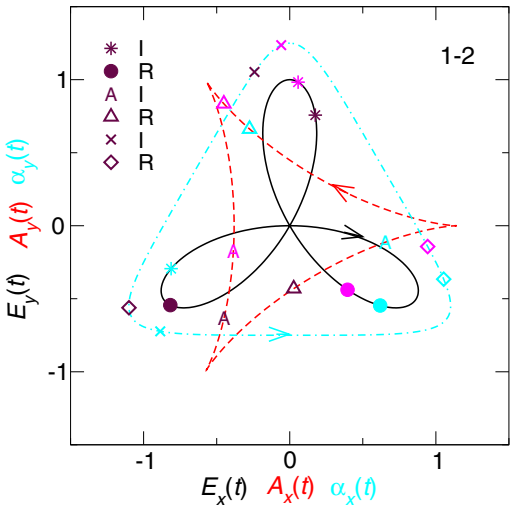

FIG. 19. Vectors $\mathbf{E}(t)$, $\mathbf{A}(t)$, and $\boldsymbol{\alpha}(t)$, presented as in Fig. 12. The ionization times (I) and rescattering times (R) for those electron trajectories that correspond to the solid lines in Fig. 18 are denoted by the corresponding symbols having the same color, as explained in the legend.

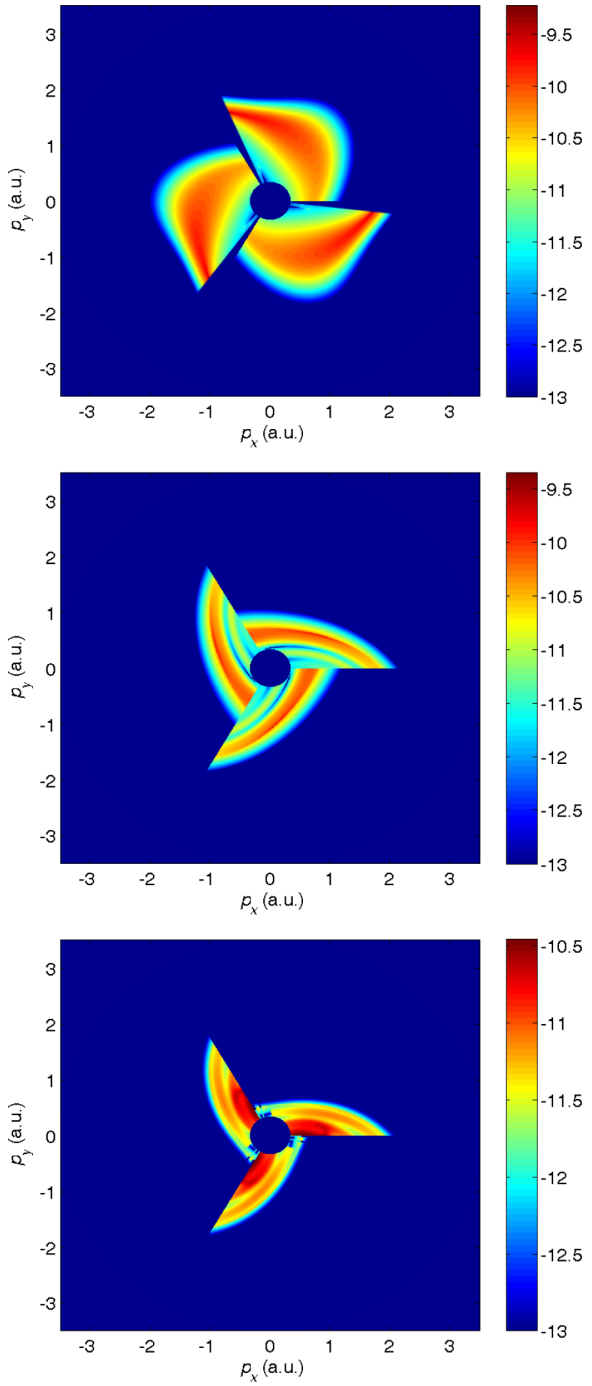

FIG. 20. Same as in Fig. 10 but obtained using the SPM with the solutions $(\nu,\rho,\mu) = (1,0,0)$ (top), $(\nu,\rho,\mu) = (\pm1,2,0)$ (middle), and $(\nu,\rho,\mu) = (\pm1,3,0)$ (bottom).

In Fig. 18 we show the electron trajectories for various forward-scattering-like saddle-point solutions. For the solutions $(\nu,\rho,\mu) = (\pm1,0,0)$, presented by the solid maroon lines for the electron energy $E_{\mathbf{p}} = 1.6U_p$, the electron moves directly from the tunnel exit to the parent ion and forward scatters off it. The trajectories for the solutions $(\nu,\rho,\mu) = (\pm1,2,0)$ are presented by solid and dot-dashed cyan lines and correspond to the energy $0.8U_p$. In this case, in order to reach the detector, which is positioned at the angle 50° with respect to the x axis, the electron has to (forward) scatter by the angle ≈60° (cyan curve). In the upper part of the figure it can be noticed that the field once more changes its direction, so the cyan trajectories are further modified. The trajectories for the solution $(\pm1,3,0)$ (solid and dashed magenta lines and the energy $0.56U_p$) are slightly longer: The electron first moves away from the origin, turns around, returns, and forward scatters off the parent ion. After rescattering, on its way to the detector, the electron for the solutions $(\pm1,3,0)$ (magenta lines) changes its direction once again, as it does for the solutions $(\pm1,2,0)$ (cyan lines).

A complete picture of the process can be inferred from Fig. 19, where we present the vectors $\mathbf{E}(t)$, $\mathbf{A}(t)$, and $\boldsymbol{\alpha}(t)$. On each of their parametric plots we have marked the ionization and rescattering times for the solutions (1,0,0), (1,2,0), and (1,3,0). The behavior of the trajectories can be completely matched with this information. We will be content with just emphasizing that for the solution (1,0,0) the field between the ionization time (maroon star) and the forward-scattering time (maroon filled circle) forms an almost linear segment. Similarly, the corresponding vector $\boldsymbol{\alpha}(t)$ follows a linear line from the cross to the diamond. To a lesser degree, this also holds true for the solution (1,2,0) between the ionization time (cyan star) and the rescattering time (cyan solid circle). However, for the solution (1,3,0) (magenta symbols) the field traces out two such almost linear segments that are rotated by the angle 120° one with respect to the other. The consequences are obvious in the trajectory exhibited in Fig. 18.

In Fig. 20 we present the velocity maps obtained using Eq. (30) for the same pairs of quantum orbits (ν,ρ,μ) that already were under scrutiny in Figs. 18 and 19. The contributions of the solutions $(\nu,\rho,\mu) = (1,0,0)$ and $(\nu,\rho,\mu) = (\pm1,2,0)$ are dominant for intermediate energies, while that of $(\pm1,3,0)$ is less important. Finally, in Fig. 21 we present the coherent sum of the forward-scattering-orbit contributions $(\nu,\rho,\mu) = (1,0,0)$ and $(\nu,\rho,\mu) = (\pm1,2,0)$ along with the contributions of the backward-scattering orbits $(\alpha,\beta,m) = (\pm1,1,0)$. The latter was already separately depicted in Fig. 10. We notice that the contributions of just five orbits are sufficient to reproduce

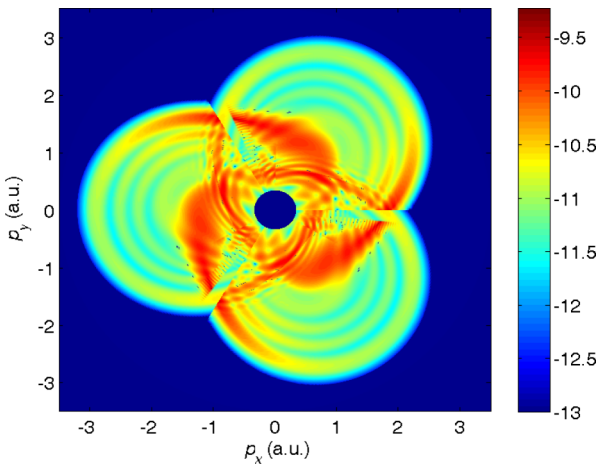

FIG. 21. Same as in Fig. 10 but obtained using the SPM with the coherent sum of the solutions $(\alpha,\beta,m) = (\pm1,1,0)$, $(\nu,\rho,\mu) = (1,0,0)$, and $(\nu,\rho,\mu) = (\pm1,2,0)$.

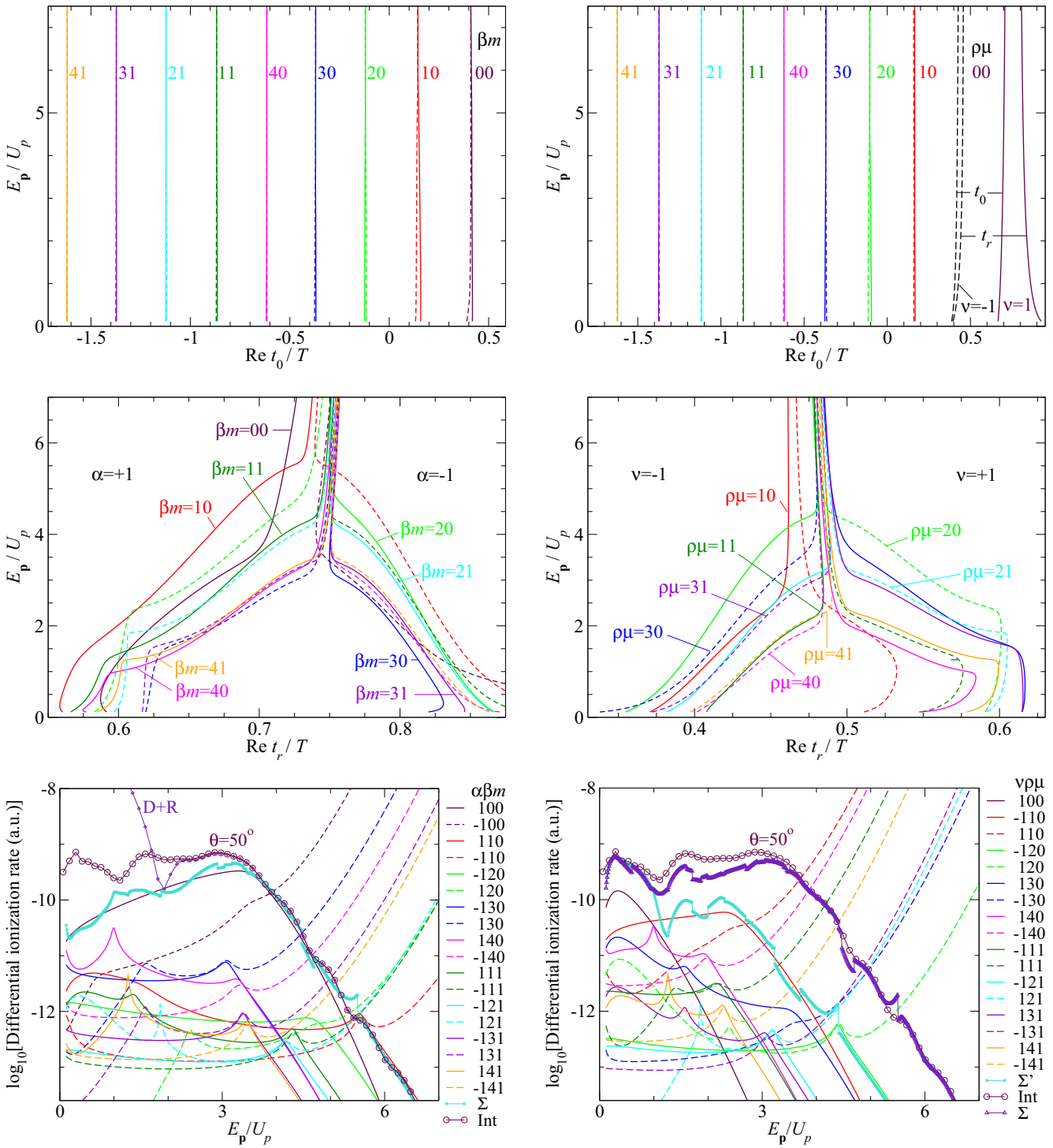

FIG. 22. Classification of the backward-scattering-like (α,β,m) (left panels) and forward-scattering-like (ν,ρ,μ) (right panels) saddle-point solutions for the ionization time (top panels) and the rescattering time (middle panels) for the ω-3ω bicircular field presented similarly and for the same parameters as in Fig. 8. The corresponding spectra are shown in the bottom panels, which are the analogs of Fig. 9. The spectrum that includes both the direct and the rescattered electron, obtained by numerical integration, is presented by small diamonds and denoted by $D+R$. In the bottom right panel the spectrum obtained as a coherent sum of the relevant contributions of the (ν,ρ,μ) solutions is denoted by Σ', while the sum that corresponds to both solutions (ν,ρ,μ) and (α,β,m) is denoted by Σ.

the velocity map of Fig. 5, which was obtained by numerical integration. In addition, we can attribute specific orbits to particular areas of the velocity map.

D. Quantum-orbit results for the bicircular ω-3ω field

Similarly to the ω-2ω field analyzed above, we can consider an arbitrary $r\omega$-$s\omega$ bicircular field. In this subsection, as an

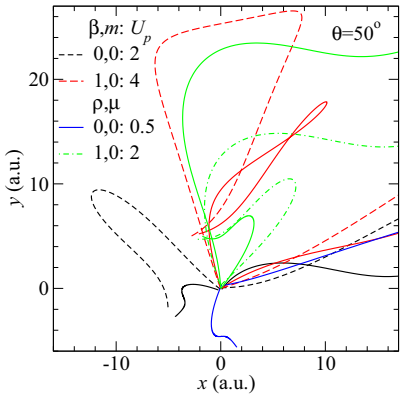

FIG. 23. Electron trajectories for some of the quantum orbits at the given energies. Laser and atomic parameters are as in previous figures.

illustration, we consider the ω-3ω bicircular field case. The corresponding classification of the saddle-point solutions and the partial ionization rates is shown in Fig. 22. From the top left panel we see that for $m = 0$ we have four solutions $\beta = 1,2,3,4$ having $-0.75 < \mathrm{Re}\, t_0/T < 0.25$, while for $m = 1$ these solutions are in the interval $-1.75 < \mathrm{Re}\, t_0/T < -0.75$. From the middle left panel it follows that all these backward-scattering-like solutions have $\mathrm{Re}\, t_r$ near $3T/4$ for the ω-3ω bicircular field (for the ω-2ω bicircular field, $\mathrm{Re}\, t_r$ was around $2T/3$, while for linear polarization it was around $T/2$). A similar classification can be adopted for the general $r\omega$-$s\omega$ field. In this case we have $\alpha = \pm 1$, $\beta = 1,2,\ldots,r+s$, $m = 0,1,2,\ldots$ and the solutions $\mathrm{Re}\, t_r$ are around $sT/(r+s)$.

Even more than in the ω-2ω case, a bewildering multitude of orbits contributes. However, only a few of them make substantial contributions. Most importantly, as demonstrated

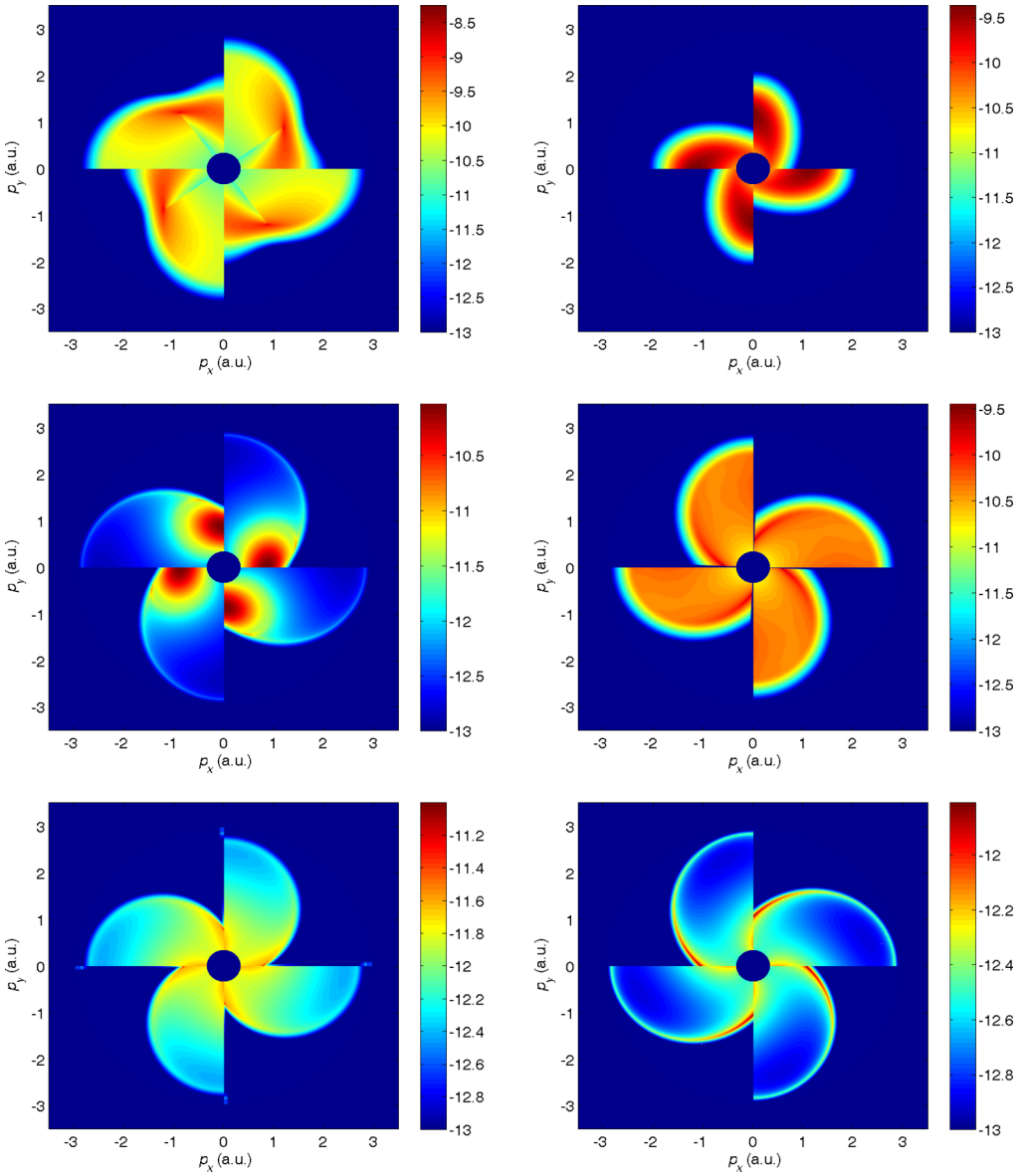

FIG. 24. Same as in Fig. 10 but for the bicircular ω-3ω field. Shown on the left are the backward-scattering-like solutions $(\alpha,\beta,m) = (1,0,0)$ (top), $(1,1,0)$ (middle), and $(-1,2,0)$ (bottom). Shown on the right are the forward-scattering-like solutions $(\nu,\rho,\mu) = (1,0,0)$ (top), $(-1,1,0)$ (middle), and $(-1,2,0)$ (bottom). Notice the different color codes of each panel.

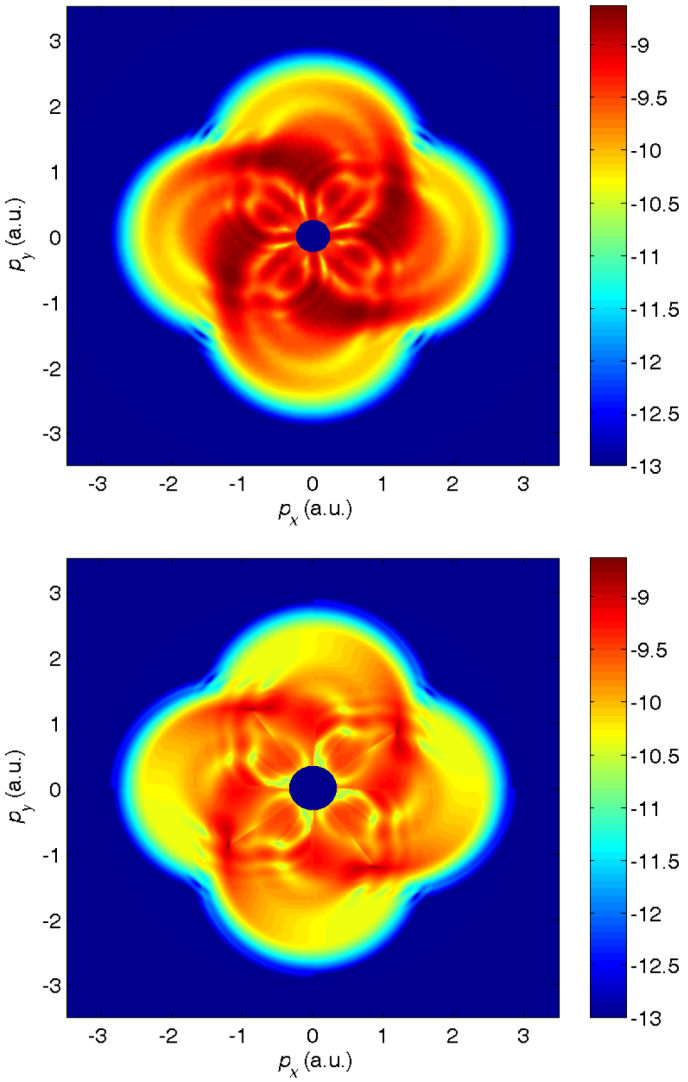

FIG. 25. Comparison of the velocity maps obtained by numerical integration (top) and using the coherent sum of only four SPM solutions: $(\alpha,\beta,m) = (1,0,0)$ and $(1,1,0)$ and $(\nu,\rho,\mu) = (1,0,0)$ and $(-1,1,0)$ (bottom). The laser and atomic parameters are as in Fig. 24.

by the blue solid curve (denoted by Σ) in the bottom right panel of Fig. 22, the result obtained by numerical integration is well approximated by the coherent sum of the quantum-orbit contributions. This is especially so for $E_{\mathbf{p}} > 3U_p$ and $< 1U_p$. Below $3U_p$ the contribution of the forward-scattering-like orbits is essential. From the bottom left panel of Fig. 22 we see that for energies between $3U_p$ and $5U_p$ the orbit $(\alpha,\beta,m) = (1,0,0)$ is completely dominant. Above $5U_p$ the orbit $(1,1,0)$ takes over the leading role. The contribution of all other (α,β,m) orbits is small for the chosen angle $\theta = 50^\circ$.

The classification of the solutions (ν,ρ,μ) and the corresponding spectra for the ω-3ω bicircular-field case are presented in the right panels of Fig. 22. From the bottom right panel we see that the spectrum below $1U_p$ is well described by the coherent sum of the contributions of the forward-scattering-like saddle-point solutions $(\nu,\rho,\mu) = (1,0,0)$ and $(-1,1,0)$. The spectrum from $1U_p$ to $3U_p$ is slightly lower than that obtained by numerical integration but is qualitatively reproduced.

In Fig. 23 we present the electron trajectories for the four quantum orbits (α,β,m) with $\alpha = \pm 1$, $\beta = 0,1$, and $m = 0$ and the three orbits $(\nu,\rho,\mu) = (1,0,0)$ and $(\pm 1,1,0)$. The trajectory of the orbit $(\beta,m) = (0,0)$ after ionization approximately follows the direction 135°, returns in the parallel direction, and rescatters at the origin by the angle ≈45°. The trajectories for $(\beta,m) = (1,0)$ are more complicated and the electron rescatters by the angle ≈90°. On the other hand, for the orbit $(\rho,\mu) = (0,0)$ the rescattering angle is ≈30°, while for $(\rho,\mu) = (1,0)$ it is about 135°.

In Fig. 24 we present the differential ionization rate in the momentum plane for the six most important saddle-point solutions. By comparison with the numerical integration result, which is shown in Fig. 25, we see that only four of them are enough to describe the spectrum qualitatively. Therefore, we have developed a detailed physical view of the space-time history of an electron emitted with a certain momentum. This approach can be generalized to an arbitrary $r\omega$-$s\omega$ bicircular field.

V. CONCLUSION

We have developed and applied the modified SPM with the asymptotic bound states to the (I)SFA. The agreement of our simple result, which includes a sum over the saddle points of an analytical expression, with the result obtained using the exact wave functions and numerical integration is very good (see the right-hand panel of Fig. 3 for the direct electrons and the high-energy part of Fig. 9 and the bottom panels of Fig. 22 for the rescattered electrons). The results obtained are applied to the calculation of the (H)ATI spectra generated by a strong bicircular field. Such fields are of significant recent interest because of the polarization properties of their high-order harmonics. The high-energy electron spectra due to the application of such a field are obtained and successfully explained using the introduced quantum-orbit theory. In particular, a previously introduced classification of the high-energy saddle-point solutions for a linearly polarized field in terms of a multiple index (α,β,m) is generalized to the bicircular field. Instead of two values, the index β now takes on the values $\beta = 1,2,\ldots,r+s$ for the case of an $r\omega$-$s\omega$ bicircular field. Particular low-energy orbits, which should appear for an arbitrary laser field, are now characterized by the multiple index $(\alpha,\beta,m) = (\pm 1,0,0)$. In addition, we have established the analog of the low-energy orbits (ν,μ) for the linearly polarized field. In this case we introduced the index ρ, which is the analog of the index β, which was used for the backscattering orbits. The orbit $(\nu,\rho,\mu) = (1,0,0)$ is especially important. The corresponding trajectory goes from the exit of the tunnel directly to the parent ion where it forward scatters. Due to the Coulomb potential, the corresponding rate is very strongly enhanced, so this orbit dominates the observed spectra in the low-energy region. Moreover, we have discovered many more orbits that contribute to the same energy region.

We emphasize that the quantum-orbit method is, in principle, very straightforward. For specified final momentum of

the released electron, it requires nothing more than finding the complex solutions of a set of two equations (the saddle-point equations). However, since there are many solutions, retrieving all of them and assessing their respective significance is not always straightforward in practice. For the bicircular field, since it evolves in a plane, it is much more complicated than for linear polarization. Still, the bottom line is the same: Very few orbits suffice to provide a good description of the exact spectrum (calculated completely numerically); see Figs. 21 and 25. The attractive feature of the quantum-orbit approach is that it comes with an intuitive space-time picture of how an electron having tunneled to freedom makes its way toward the detector where it is to arrive with specified momentum. This picture strongly depends upon the value of the final momentum. There may be more than one orbit that leads into the same final state, and their contributions will interfere.

For example, consider the velocity map in the top left panel of Fig. 5, which is calculated completely numerically, and its approximation in Fig. 21 by the coherent sum of a finite number of quantum orbits. Let us compare this with the contributions of individual quantum orbits exhibited in Figs. 10 and 20. This allows one to relate particular features of the velocity map to specific quantum orbits. Ideally, an experimental velocity map should be compared in this fashion with specific quantum orbits. Since each orbit corresponds to a well-defined space-time trajectory with specified start time and return time, this offers the potential for unlimited control, by inhibiting or enhancing ionization or rescattering at these times by the application of ultrashort UV pulses or fields that are perpendicular to the plane of polarization of the bicircular field, as it was realized, e.g., in Ref. [79]. High-order harmonic emission could be controlled in the same way. Above-threshold ionization has the big advantage over HHG that experiments access the single-atom dynamics.

Finally, the rescattered electrons can have the same final momentum as the direct electrons, which gives rise to the interference effect known as strong-field photoelectron holography. It was first observed for strong-field ionization by a linearly polarized laser field [80,81]. The same effect should exist for a bicircular field. However, since in this case the electron trajectories develop in a plane, the structures that correspond to direct electrons and forward-scattered electrons can be well separated [43]. This will make the holographic structures even more interesting, but adds to the complexity of their analysis. We leave the strong-bicircular-field photoelectron holography for future investigation.

[1] P. Agostini and L. F. DiMauro, Rep. Prog. Phys. **67**, 813 (2004).
[2] A. Scrinzi, M. Y. Ivanov, R. Kienberger, and D. M. Villeneuve, J. Phys. B **39**, R1 (2006).
[3] D. B. Milošević, G. G. Paulus, D. Bauer, and W. Becker, J. Phys. B **39**, R203 (2006).
[4] F. Krausz and M. Ivanov, Rev. Mod. Phys. **81**, 163 (2009).
[5] M. Nisoli and G. Sansone, Prog. Quantum Electron. **33**, 17 (2009).
[6] K. Ueda and K. L. Ishikawa, Nat. Phys. **7**, 371 (2011).
[7] P. Agostini and L. F. DiMauro, Adv. At. Mol. Opt. Phys. **61**, 117 (2012).
[8] M. Kohler, T. Pfeifer, K. Hatsagortsyan, and C. Keitel, Adv. At. Mol. Opt. Phys. **61**, 159 (2012).
[9] P. Salières, A. Maquet, S. Haessler, J. Caillat, and R. Taïeb, Rep. Prog. Phys. **75**, 062401 (2012).
[10] W. Becker, X. Liu, P. J. Ho, and J. H. Eberly, Rev. Mod. Phys. **84**, 1011 (2012).
[11] A. S. Landsman and U. Keller, Phys. Rep. **547**, 1 (2015).
[12] B. Wolter, M. G. Pullen, M. Baudisch, M. Sclafani, M. Hemmer, A. Senftleben, C. D. Schröter, J. Ullrich, R. Moshammer, and J. Biegert, Phys. Rev. X **5**, 021034 (2015).
[13] R. Pazourek, S. Nagele, and J. Burgdörfer, Rev. Mod. Phys. **87**, 765 (2015).
[14] P. B. Corkum, Phys. Rev. Lett. **71**, 1994 (1993).
[15] P. Salières, B. Carré, L. Le Déroff, F. Grasbon, G. G. Paulus, H. Walther, R. Kopold, W. Becker, D. B. Milošević, A. Sanpera, and M. Lewenstein, Science **292**, 902 (2001).
[16] D. B. Milošević, D. Bauer, and W. Becker, J. Mod. Opt. **53**, 125 (2006).
[17] D. B. Milošević, J. Math. Phys. **54**, 042101 (2013).
[18] D. B. Milošević, in *Ultrafast Dynamics Driven by Intense Light Pulses. From Atoms to Solids, from Lasers to Intense X-rays*, edited by M. Kitzler and S. Gräfe, Springer Series on Atomic, Optical, and Plasma Physics, Vol. 86 (Springer, Basel, 2016), Chap. 2.
[19] R. Kopold, W. Becker, and M. Kleber, Opt. Commun. **179**, 39 (2000).
[20] R. Kopold, D. B. Milošević, and W. Becker, Phys. Rev. Lett. **84**, 3831 (2000).
[21] D. B. Milošević and W. Becker, Phys. Rev. A **66**, 063417 (2002).
[22] W. Becker, F. Grasbon, R. Kopold, D. B. Milošević, G. G. Paulus, and H. Walther, Adv. At. Mol. Opt. Phys. **48**, 35 (2002).
[23] D. B. Milošević, J. Phys. B **33**, 2479 (2000).
[24] H. Eichmann, A. Egbert, S. Nolte, C. Momma, B. Wellegehausen, W. Becker, S. Long, and J. K. McIver, Phys. Rev. A **51**, R3414 (1995).
[25] S. Long, W. Becker, and J. K. McIver, Phys. Rev. A **52**, 2262 (1995).
[26] T. Zuo and A. D. Bandrauk, J. Nonlinear Opt. Phys. Mater. **04**, 533 (1995).
[27] D. B. Milošević, W. Becker, and R. Kopold, Phys. Rev. A **61**, 063403 (2000); D. B. Milošević, W. Becker, R. Kopold, and W. Sandner, Laser Phys. **11**, 165 (2001).
[28] D. B. Milošević and W. Sandner, Opt. Lett. **25**, 1532 (2000).
[29] D. B. Milošević and W. Becker, Phys. Rev. A **62**, 011403(R) (2000); J. Mod. Opt. **52**, 233 (2005).
[30] D. B. Milošević, W. Becker, and R. Kopold, in *Proceedings of the Conference on Atoms, Molecules and Quantum Dots in Laser Fields: Fundamental Processes*, edited by N. Bloembergen, N. Rahman, and A. Rizzo (Società Italiana di Fisica, Bologna, 2001), Vol. 71, pp. 239–252.
[31] A. Fleischer, O. Kfir, T. Diskin, P. Sidorenko, and O. Cohen, Nat. Photon. **8**, 543 (2014).

[32] E. Pisanty and M. Ivanov, Nat. Photon. **8**, 501 (2014); E. Pisanty, S. Sukiasyan, and M. Ivanov, Phys. Rev. A **90**, 043829 (2014).
[33] O. Kfir *et al.*, Nat. Photon. **9**, 99 (2015).
[34] D. B. Milošević, Opt. Lett. **40**, 2381 (2015).
[35] D. B. Milošević, J. Phys. B **48**, 171001 (2015).
[36] L. Medišauskas, J. Wragg, H. van der Hart, and M. Yu. Ivanov, Phys. Rev. Lett. **115**, 153001 (2015).
[37] D. B. Milošević, Phys. Rev. A **92**, 043827 (2015).
[38] T. Fan *et al.*, Proc. Natl. Acad. Sci. U.S.A. **112**, 14206 (2015).
[39] A picture related to the bicircular field was chosen as the cover page of Science **348** (6234) (2015); see also J. Miao, T. Ishikawa, I. K. Robinson, and M. M. Murnane, Science **348**, 530 (2015).
[40] C. Chen *et al.*, Sci. Adv. **2**, e1501333 (2016).
[41] E. Hasović, D. B. Milošević, and W. Becker, Laser Phys. Lett. **3**, 200 (2006).
[42] A. Kramo, E. Hasović, D. B. Milošević, and W. Becker, Laser Phys. Lett. **4**, 279 (2007); E. Hasović, A. Kramo, and D. B. Milošević, Eur. Phys. J. Spec. Top. **160**, 205 (2008).
[43] C. A. Mancuso, D. D. Hickstein, P. Grychtol, R. Knut, O. Kfir, X.-M. Tong, F. Dollar, D. Zusin, M. Gopalakrishnan, C. Gentry, E. Turgut, J. L. Ellis, M.-C. Chen, A. Fleischer, O. Cohen, H. C. Kapteyn, and M. M. Murnane *et al.*, Phys. Rev. A **91**, 031402(R) (2015).
[44] E. Hasović, W. Becker, and D. B. Milošević, Opt. Express **24**, 6413 (2016).
[45] C. A. Mancuso, D. D. Hickstein, K. M. Dorney, J. L. Ellis, E. Hasović, R. Knut, P. Grychtol, C. Gentry, M. Gopalakrishnan, D. Zusin, F. J. Dollar, X.-M. Tong, D. B. Milošević, W. Becker, H. C. Kapteyn, and M. M. Murnane, Phys. Rev. A **93**, 053406 (2016).
[46] C. I. Blaga, F. Catoire, P. Colosimo, G. G. Paulus, H. G. Muller, P. Agostini, and L. F. DiMauro, Nat. Phys. **5**, 335 (2009).
[47] W. Quan, Z. Lin, M. Wu, H. Kang, H. Liu, X. Liu, J. Chen, J. Liu, X. T. He, S. G. Chen, H. Xiong, L. Guo, H. Xu, Y. Fu, Y. Cheng, and Z. Z. Xu, Phys. Rev. Lett. **103**, 093001 (2009).
[48] L. Guo, S. S. Han, X. Liu, Y. Cheng, Z. Z. Xu, J. Fan, J. Chen, S. G. Chen, W. Becker, C. I. Blaga, A. D. DiChiara, E. Sistrunk, P. Agostini, and L. F. DiMauro, Phys. Rev. Lett. **110**, 013001 (2013).
[49] M. Möller, F. Meyer, A. M. Sayler, G. G. Paulus, M. F. Kling, B. E. Schmidt, W. Becker, and D. B. Milošević, Phys. Rev. A **90**, 023412 (2014).
[50] W. Becker and D. B. Milošević, J. Phys. B **48**, 151001 (2015).
[51] W. Becker, S. P. Goreslavski, D. B. Milošević, and G. G. Paulus, J. Phys. B **47**, 204022 (2014).
[52] D. B. Milošević, Phys. Rev. A **90**, 063414 (2014).
[53] W. Becker and D. B. Milošević, Chin. Opt. Lett. **13**, 070006 (2015).
[54] D. B. Milošević, Phys. Rev. A **90**, 063423 (2014).
[55] E. Clementi and C. Roetti, At. Data Nucl. Data Tables **14**, 177 (1974); A. D. McLean and R. S. McLean, *ibid.* **26**, 197 (1981); C. F. Bunge, J. A. Barrientos, and A. V. Bunge, *ibid.* **53**, 113 (1993).
[56] A. A. Radzig and B. M. Smirnov, *Reference Data on Atoms, Molecules and Ions* (Springer, Berlin, 1985).
[57] G. F. Gribakin and M. Y. Kuchiev, Phys. Rev. A **55**, 3760 (1997).
[58] D. B. Milošević, A. Gazibegović-Busuladžić, and W. Becker, Phys. Rev. A **68**, 050702(R) (2003); A. Gazibegović-Busuladžić, D. B. Milošević, and W. Becker, *ibid.* **70**, 053403 (2004).
[59] X. M. Tong, Z. X. Zhao, and C. D. Lin, Phys. Rev. A **66**, 033402 (2002).
[60] T. K. Kjeldsen and L. B. Madsen, Phys. Rev. A **71**, 023411 (2005).
[61] D. B. Milošević, Phys. Rev. A **93**, 051402(R) (2016), showed that it is possible to introduce spin into attoscience with spin-polarized electrons produced by a bicircular laser field.
[62] S. F. C. Shearer and S. M. K. Law, J. Phys. B **48**, 055402 (2015).
[63] L. V. Keldysh, Zh. Eksp. Teor. Fiz. **47**, 1945 (1964) [Sov. Phys. JETP **20**, 1307 (1965)]; F. H. M. Faisal, J. Phys. B **6**, L89 (1973); H. R. Reiss, Phys. Rev. A **22**, 1786 (1980).
[64] D. B. Milošević and F. Ehlotzky, J. Phys. B **31**, 4149 (1998); Phys. Rev. A **58**, 3124 (1998); J. Phys. B **32**, 1585 (1999).
[65] D. B. Milošević, Phys. Rev. A **88**, 023417 (2013).
[66] E. Hasović, M. Busuladžić, A. Gazibegović-Busuladžić, D. B. Milošević, and W. Becker, Laser Phys. **17**, 376 (2007).
[67] T. K. Kjeldsen and L. B. Madsen, Phys. Rev. A **74**, 023407 (2006).
[68] C. P. J. Martiny, Strong-field ionization of atoms and molecules by short femtosecond laser pulses, Ph.D. thesis, Aarhus University, 2010.
[69] D. B. Milošević, E. Hasović, M. Busuladžić, A. Gazibegović-Busuladžić, and W. Becker, Phys. Rev. A **76**, 053410 (2007).
[70] S. Odžak and D. B. Milošević, Phys. Rev. A **72**, 033407 (2005).
[71] S. Odžak and D. B. Milošević, Phys. Rev. A **92**, 053416 (2015).
[72] H. B. van Linden van den Heuvell and H. G. Muller, in *Multiphoton Processes*, edited by S. J. Smith and P. L. Knight, Cambridge Studies of Modern Optics (Cambridge University Press, Cambridge, 1988), Vol. 8, p. 25.
[73] M. Lewenstein, P. Balcou, M. Y. Ivanov, A. L'Huillier, and P. B. Corkum, Phys. Rev. A **49**, 2117 (1994).
[74] This notation is slightly different from that of Refs. [21,69], where we had $\beta = \pm 1$ for the linearly polarized field case, which corresponds to $\beta = 1,2$ in the present case. The meaning of the index m is also slightly different (for example, the red dotted line has carried the index $m = 1$ in previous notation). Previous notation $(\beta,m) = \{(-1,0),(1,1),(-1,1),(1,2),\ldots\}$ is now replaced by $(\beta,m) = \{(1,0),(2,0),(1,1),(2,1),\ldots\}$. Now, for each $m = 0,1,\ldots$ there are two pairs of solutions having the real part of the ionization time t_0 between $-(m+1)T$ and mT.
[75] The solutions $(\alpha,\beta,m) = (\pm 1,0,0)$ will be considered separately. These solutions are analogous to the $(\alpha,\beta,m) = (\pm 1,1,0)$ solutions that were discovered in Ref. [52] for the linearly polarized field case. They do not contribute to the high-energy electrons and their physical meaning is described by the formalism of the complex quantum orbits [52]. Since they are unique we use only the value $\beta = 0$ of the index β instead of the values $\beta = 1,2,3$, which we use for other solutions.
[76] C. Figueira de Morisson Faria, H. Schomerus, and W. Becker, Phys. Rev. A **66**, 043413 (2002).
[77] A. N. Pfeiffer, C. Cirelli, M. Smolarski, R. Dörner, and U. Keller, Nat. Phys. **7**, 428 (2011).
[78] A. Kästner, U. Saalmann, and J. M. Rost, Phys. Rev. Lett. **108**, 033201 (2012); J. Phys. B **45**, 074011 (2012).
[79] M. Richter, M. Kunitski, M. Schöffler, T. Jahnke, L. P. H. Schmidt, M. Li, Y. Liu, and R. Dörner, Phys. Rev. Lett. **114**, 143001 (2015).
[80] Y. Huismans *et al.*, Science **331**, 61 (2011).
[81] X.-B. Bian, Y. Huismans, O. Smirnova, K.-J. Yuan, M. J. J. Vrakking, and A. D. Bandrauk, Phys. Rev. A **84**, 043420 (2011).